

Chandra and Spitzer unveil heavily obscured quasars in the SWIRE/Chandra Survey¹

Maria del Carmen Polletta², Belinda J. Wilkes³, Brian Siana^{4,5}, Carol J. Lonsdale^{2,6}, Roy Kilgard³, Harding E. Smith^{2,5}, Dong-Woo Kim³, Frazer Owen^{5,7}, Andreas Efstathiou⁸, Tom Jarrett⁶, Gordon Stacey⁹, Alberto Franceschini¹⁰, Michael Rowan-Robinson¹¹, Tom S.R. Babbedge¹¹, Stefano Berta¹⁰, Fan Fang⁴, Duncan Farrah⁹, Eduardo González-Solares¹², Glenn Morrison^{5,13}, Jason A. Surace⁴, Dave L. Shupe⁴

mcp@auriga.ucsd.edu

ABSTRACT

Using the large multi-wavelength data set in the *Chandra*/SWIRE Survey (0.6 deg^2 in the Lockman Hole), we show evidence for the existence of highly obscured (Compton-thick) AGN, estimate a lower limit to their surface density and characterize their multi-wavelength properties. Two independent selection methods based on the X-ray and infrared spectral properties are presented. The two selected samples contain 1) 5 X-ray sources with hard X-ray spectra and column densities $\gtrsim 10^{24} \text{ cm}^{-2}$, and 2) 120 infrared sources with red and AGN-dominated infrared spectral energy distributions (SEDs). We estimate a surface density of at least 25 Compton-thick AGN deg^{-2} detected in the infrared in the *Chandra*/SWIRE field of which $\sim 40\%$ show distinct AGN signatures in their optical/near-infrared SEDs, the remainings being dominated by the host-galaxy emission. Only $\sim 33\%$ of all Compton-thick AGN are detected in the X-rays at our depth ($F(0.3\text{-}8 \text{ keV}) > 10^{-15} \text{ ergs cm}^{-2} \text{ s}^{-1}$).

We report the discovery of two sources in our sample of Compton-thick AGN, SWIRE_J104409.95+585224.8 ($z=2.54$) and SWIRE_J104406.30+583954.1 ($z=2.43$), which are the most luminous Compton-thick AGN at high- z currently known. The properties of these two sources are discussed in detail with an analysis of their spectra, SEDs, luminosities and black-hole masses.

Subject headings: galaxies: active — quasars: individual (SWIRE_J104409.95+585224.8, SWIRE_J104406.30+583954.1) — infrared: galaxies — X-rays: galaxies

¹Some of the data presented herein were obtained at the W.M. Keck Observatory, which is operated as a scientific partnership among the California Institute of Technology, the University of California and the National Aeronautics and Space Administration. The Observatory was made possible by the generous financial support of the W.M. Keck Foundation. Based on observations at the Kitt Peak National Observatory, National Optical Astronomy Observatory, which is operated by the Association of Universities for Research in Astronomy, Inc. under cooperative agreement with the National Science Foundation. The National Radio Astronomy Observatory is a facility of the National Science Foundation operated under a cooperative agreement by Associated Universities Inc.

²Center for Astrophysics & Space Sciences, University

of California, San Diego, La Jolla, CA 92093, USA

³Harvard/Smithsonian Center for Astrophysics, 60 Garden Street, Cambridge, MA 02138, USA

⁴Spitzer Science Center, California Institute of Technology, 100-22, Pasadena, CA 91125, USA

⁵Visiting astronomer, Kitt Peak National Observatory, National Optical Astronomy Observatories, operated by AURA Inc, under cooperative agreement with the National Science Foundation.

⁶Infrared Processing & Analysis Center, California Institute of Technology, 100-22, Pasadena, CA 91125, USA

⁷National Radio Astronomy Observatory[‡], P.O. Box O, Socorro, NM 87801, USA

⁸School of Computer Science and Engineering, Cyprus

1. Introduction

According to the AGN unification models (Antonucci 1993; Krolik 1999), all AGN are intrinsically similar, and the observational differences among various types are due to the geometry and orientation with respect to the line of sight of obscuring matter surrounding the central supermassive black hole (SMBH). According to this model, obscuring matter is ubiquitous in AGN, but the effects of absorption are only seen when the line of sight intercepts it. Alternative models attribute the presence of obscuration to a stage in the early phases of AGN evolution during a merger (Fabian 1999). Mergers of large disk galaxies hosting a SMBH induce the growth of the SMBH and of the host galaxy spheroid throughout vigorous star-formation episodes. During this phase the AGN is surrounded by large amounts of gas and dust, thus it appears as heavily obscured. As the AGN reaches a certain luminosity, its radiation can cause the expulsion and destruction of the surrounding material and the system appears as an unobscured AGN (Silk & Rees 1998; Granato et al. 2004; Springel et al. 2005; Hopkins et al. 2005; Di Matteo et al. 2005; Cattaneo et al. 2005).

Since AGN that are not affected by obscuration are relatively easy to detect and identify across the entire wavelength spectrum, they have been well sampled up to high redshifts and their properties, space density, luminosity function and redshift distributions are well measured (Ueda et al. 2003; Richards et al. 2005). On the other hand, AGN obscured by even only moderate column densities ($N_{\text{H}} \simeq 10^{22} \text{ cm}^{-2}$) (Richards et al. 2003; White et al. 2003), are routinely missed in observations at various wavelengths because of the difficulty of detecting and identifying them, and, therefore, they

College, 6 Diogenes Street, Engomi, 1516 Nicosia, Cyprus

⁹Department of Astronomy, Cornell University, Ithaca, NY 14853, USA

¹⁰Dipartimento di Astronomia, Università di Padova, Via del Osservatorio 2, I-35122, Padova, Italy

¹¹Astrophysics Group, Blackett Lab., Imperial College, Prince Consort Road, London, SW7 2BW, UK

¹²Institute of Astronomy, University of Cambridge, Madingley Road, Cambridge, CB3 0HA, UK

¹³Institute for Astronomy, University of Hawaii, and Canada-France-Hawaii Telescope, Kamuela, Hawaii 96743-8432, USA

are not as well understood. There is evidence that obscured AGN are numerous and might even outnumber unobscured AGN, however optically and X-ray selected samples of AGN are still dominated by unobscured AGN and large and complete samples of obscured AGN are still missing providing only few observables to constrain models.

1.1. Indirect evidence for the existence of highly obscured AGN

In the local Universe and for moderate (Seyfert-like) nuclear luminosities ($< 10^{44} \text{ ergs s}^{-1}$), the observed ratio between obscured ($N_{\text{H}} > 10^{22} \text{ cm}^{-2}$) and unobscured ($N_{\text{H}} < 10^{22} \text{ cm}^{-2}$) AGN is 4:1 (Osterbrock & Shaw 1988; Madau, Ghisellini, & Fabian 1994; Comastri et al. 1995; Risaliti et al. 1999; Piconcelli et al. 2003) and $\sim 45\%$ of the obscured ones are Compton-thick (column density larger than 10^{24} cm^{-2}) (Risaliti et al. 1999; Maiolino & Rieke 1995). Large column densities ($\sim 10^{24} \text{ cm}^{-2}$) have been directly measured only in a few, ~ 10 , sources (e.g. NGC1068, Circinus, NGC4945). For most of the known Compton-thick AGN, ~ 40 (Comastri 2004), only indirect evidence to their extreme column densities is available (Bassani et al. 1999; Risaliti et al. 1999; Maiolino et al. 2003), such as the flatness of the hard X-ray continuum, a large equivalent width (EW) of the $K_{\alpha} 6.4 \text{ keV}$ iron fluorescent emission line, or lower than expected values of the ratio between the flux in the X-rays and in other wavelengths. At higher-redshift (> 1) and luminosities ($\geq 10^{44} \text{ ergs s}^{-1}$), the distribution of absorption in AGN is not as well constrained with only a few examples of confirmed obscured quasars. There is evidence that the fraction of obscured AGN decreases with higher intrinsic luminosities (Ueda et al. 2003; Szokoly et al. 2004; Barger et al. 2005; Treister & Urry 2005), and possibly increases with redshift (La Franca et al. 2005).

Other indications for the existence of numerous obscured AGN have been provided by AGN studies at wavelengths less affected by obscuration, such as infrared (IR) and radio. Stern et al. (2004) compared the surface density of an IR-selected sample of AGN ($F(8\mu\text{m}) > 76\mu\text{Jy}$) with that of an optically-selected (R-mag < 21) (Wolf et al. 2003) sample of AGN and found 2.8 times more AGN in the IR than in the optical sample. Since the ratio between the limiting fluxes

of the two samples corresponds to the typical R-band/8 μ m flux ratio of unobscured AGN, the higher density of IR-selected AGN is attributed to an excess of obscured AGN. Similar results were obtained from an IR and radio selected sample of AGN (Martínez-Sansigre et al. 2005) in which the fraction of obscured sources at high-redshift ($z \sim 2$) is estimated to be 50% (obscured:unobscured=1:1) or as high as 87% (obscured:unobscured=2.6:1) if sources which are not confirmed spectroscopically are also taken into account. An obscured:unobscured ratio of 2:1 was also derived from a sample of AGN selected at 24 μ m (Alonso-Herrero et al. 2005).

The existence of a large population of obscured AGN is also suggested by the shape of the X-ray background at high energies. More than 85% of the 2–10 keV Cosmic X-ray Background has been resolved by sources detected in deep X-ray surveys (Moretti et al. 2003; De Luca & Molendi 2004). However, the resolved fraction decreases at higher energies, e.g. in the 4–6 keV energy range the resolved fraction is about 70–90%, whilst in the 8–12 keV band no more than 50% is resolved. Less than 30% is resolved above 10 keV, where the bulk of the CXRB energy density is produced (Worsley et al. 2004, 2005). The spectral shape of the residual background cannot be produced by a simple superposition of unobscured AGN spectra, but by an X-ray population with faint low-energy X-ray fluxes and hard X-ray spectra, as in obscured AGN (Worsley et al. 2005).

1.2. Searches for obscured AGN

In spite of the difficulty of finding and identifying highly obscured AGN, several searches have been conducted combining multiwavelength data (Webster et al. 1995; Wilkes et al. 2002; Padovani et al. 2004; Donley et al. 2005; Stern et al. 2004; Martínez-Sansigre et al. 2005; Zakamska et al. 2004; Urrutia et al. 2005), performing very deep observations (Treister & Urry 2005; Van Duyne et al. 2004) or surveying large areas of the sky (Cutri et al. 2002; Fiore et al. 2003; Zakamska et al. 2004; Urrutia et al. 2005). Obscured AGN candidates have been selected among X-ray sources with hard X-ray spectra or with high (>10) X-ray over optical flux ratios (Fiore et al. 2003; Rigby et al. 2004), with radio emission in excess compared to the IR (Donley et al. 2005;

Urrutia et al. 2005) or with narrow emission lines in their optical spectra (Zakamska et al. 2004). These sources are predominantly characterized by column densities of the order of 10^{22} cm^{-2} and by various types of optical spectra, with narrow emission lines as expected in type 2 AGN, but also with broad emission lines, as in unobscured AGN, or typical of normal, early and late-type, galaxies (Fiore et al. 2003; Perola et al. 2004).

All these studies aimed at finding the obscured AGN population predicted by models and indirect observations have been successful to varying degrees. However, most of these sample are affected by selection effects and characterized by properties too broad to constrain models, and the measured column densities are only moderate ($N_{\text{H}}=10^{22-23} \text{ cm}^{-2}$). A common property of these moderately obscured AGN is the variety of optical/near-IR spectral energy distributions (SEDs), with only a minority of sources showing typical AGN signatures (Franceschini et al. 2005; Donley et al. 2005; Rigby et al. 2004). Consequently, any search in a specific wavelength range will provide incomplete samples of obscured AGN.

In this work, we aim at identifying and characterizing only the most obscured AGN, with column densities of the order of 10^{24} cm^{-2} , the so-called Compton-thick AGN. By looking at the most obscured AGN which are also the hardest to find because of their elusive properties, we hope to provide useful constraints on AGN models. Our analysis is based on the sources detected by *Spitzer* and *Chandra* in a wide area (0.6 deg^2) multi-wavelength (from radio to X-ray) survey performed in the Lockman Hole, the *Chandra*/SWIRE survey. This field was selected for deep follow-up observations within the *Spitzer* Wide-Area Infrared Extragalactic Survey (SWIRE) (Lonsdale et al. 2003, 2004) legacy project. By comparing samples selected independently in the X-rays and in the IR, the incompleteness level of each selection method can be estimated. The available multiwavelength data set is described in Section 2. In Section 3, we present our selection methods for heavily obscured AGN, an X-ray based selection in Section 3.1 and an IR based selection in Section 3.2. The general properties of the two samples, SEDs, X-ray over optical and mid-IR fluxes are discussed in Sections 3.2.2 and 3.2.3. A detailed analysis of the properties

of two spectroscopically confirmed Compton-thick quasars present in both samples is given in sections 4 (data description), 5 (SED analysis), and 6 (bolometric luminosity and black hole mass estimate). A comparison between our candidates and other samples of heavily obscured AGN is presented in section 7. In Section 8, we estimate a lower limit to the surface density of Compton-thick AGN detected in the IR at our sensitivity limits in the *Chandra*/SWIRE field and compare our estimates with current models. Our results are summarized in Section 9.

Throughout the paper, we adopt a flat cosmology with $H_0 = 71 \text{ km s}^{-1} \text{ Mpc}^{-1}$, $\Omega_M = 0.27$ and $\Omega_\Lambda = 0.73$ (Spergel et al. 2003).

2. Observations

The *Chandra*/SWIRE field, located in the northern part of the Lockman Hole Field (10^h45^m , $+59^\circ$), has been selected as the target for the deepest IR, optical and radio SWIRE observations, and for a moderately deep and wide *Chandra* survey. This field has the lowest cirrus sky emission of all of the SWIRE fields (0.38 MJy/sr at $100\mu\text{m}$) and has no contamination from moderate brightness radio sources, making it ideally suited for a radio-IR survey. The neutral Galactic column density toward this field is on average $6.43 \times 10^{19} \text{ cm}^{-2}$ (Dickey & Lockman 1990), making it ideal also for deep X-ray surveys. The data available in this field are summarized in Table 1 and details on the observations are given in the following sections.

2.1. Optical and Infrared Imaging Observations

Optical imaging in U , g' , r' , and i' was obtained with the Mosaic Camera at the Kitt Peak National Observatory (KPNO) Mayall 4-mt Telescope on February 2002 (g' , r' , and i') and January 2004 (U). The coverage of the field is not uniform, the central 0.3 deg^2 ($\alpha=161^\circ\text{--}162^\circ$ and $\delta=58.75^\circ\text{--}59.25^\circ$) were covered with a 3 hour exposure in g' , r' , and i' , and with a 6 hour exposure in U -band to 5σ limiting Vega magnitudes of 24.8 (U), 25.9 (g'), 25.2 (r'), and 24.4 (i'). The surrounding area at $\delta > 58.6^\circ$ was also covered in four bands with 50 min exposure in g' , and r' , 30 min exposure in i' , and with a 2 hour exposure in U -band to a depth

of 24.3 (U), 25.2 (g'), 24.4 (r'), and 23.5 (i'). The small region at $\delta < 58.6^\circ$ was observed only in the g' , r' , and i' bands with a 30 min exposure to a depth of 23.7 (g'), 23.5 (r'), and 22.9 (i'). The astrometry is good to less than 0.4 arcsec and the seeing varies between 0.9 and 1.4 arcsec. The data were processed with the Cambridge Astronomical Survey Unit's reduction pipeline following the procedures described in Babbedge (2004a). Fluxes were measured within $3''$ apertures (diameter) and corrected to total fluxes using profiles measured on bright stars. Total magnitudes, derived by integrating over the curve of growth, were adopted for sources extended and bright in the three filters g' , r' , and i' ($g' < 23.8$, $r' < 22.7$, $i' < 22.0$). The optical catalog contains 77,355 sources (galaxies and stars) of which 45,573 are detected in at least two bands.

Near-IR K_s imaging observations were carried out with the $200''$ Hale Telescope of the Palomar Observatory using the Wide Infrared Camera (WIRC; Wilson et al. (2003)) on 2004 March 29 under photometric conditions. The field was partially covered, 0.43 deg^2 , with $24 8.5'' \times 8.5''$ pointings of 72 min exposure. Data reduction for the near-IR imaging consisted of median-sky removal, flat-fielding using a median “sky” image derived from the science observations, co-addition, and astrometric and flux calibration. The seeing FWHM ranges between 0.7 and 1.3 arcsec. Sources were extracted using SExtractor (Bertin & Arnouts 1996) and MAG_BEST magnitudes were adopted. Calibration was carried out using the near-IR 2MASS Point Source Catalog (Cutri et al. 2003). The K_s -band photometric uncertainty, relative to 2MASS, is $\sim 6\%$ and the 5-sigma sensitivity is 20.5 mag (Vega). The K_s catalog contains 19,876 sources, of which 17,140 have an optical counterpart.

Observations with the Infrared Array Camera (IRAC) (Fazio et al. 2004) were performed on 2003, December 5 and 2004, April 24–30 and observations with the Multiband Imaging Photometer (MIPS) (Rieke et al. 2004) were performed on 2003, December 9 and 2004, May, 4–11. The IRAC depth was 120–480 seconds, depending on exact field location, with a median depth of 240 seconds and MIPS depth was 160–360 seconds, with a median depth of 360 seconds. Fluxes were measured using SExtractor (Bertin & Arnouts

1996) from mosaics of the flat fielded images processed by the *Spitzer* Science Center using the S11 data pipelines. Fluxes were extracted in 5.8'' diameter apertures for IRAC ($\sim 2\text{-}3 \times$ the FWHM beam) and 12'' for MIPS 24 μm using SExtractor (Bertin & Arnouts 1996) and corrected for aperture to total fluxes using the IRAC/MIPS point spread functions (PSFs). In the case of extended sources (SExtractor stellarity index < 0.8 and ISO_Area > 200) in the IRAC images, Kron fluxes were used. Details of the IRAC and MIPS data processing are given in Surace et al. (2005). The 5σ depths of the *Spitzer* data are 5, 9, 43, 40 and 230 μJy at 3.6, 4.5, 5.8, 8.0 and 24 μm , respectively. The IR catalog contains 41,262 sources, of which 31,106 have an optical counterpart.

2.2. *Chandra* X-ray Data and Analysis

We have obtained *Chandra* Advanced CCD Imaging Spectrometer (ACIS-I) (Weisskopf, O'dell, & van Speybroeck 1996) observations in a 3×3 raster of a 0.6 deg^2 region with center $\alpha = 10^{\text{h}} 46^{\text{m}}$ and $\delta = +59^{\circ} 01'$ and $\sim 2'$ overlap between contiguous pointings within the Lockman Hole field of the SWIRE survey. The exposure time for each observation was ~ 70 ksecs, reaching broad-(0.3–8 keV), soft- (0.3–2.5 keV) and hard-band (2.5–8 keV) fluxes of $\sim 10^{-15}$, 5×10^{-16} , and 10^{-14} $\text{ergs cm}^{-2} \text{s}^{-1}$, respectively. The observations were obtained on 2004, September 12–26 and processed using the XPIPE pipeline developed for analysis of *Chandra* data for the ChaMP project (Kim et al. 2004). XPIPE screens bad data, corrects instrumental effects remaining after the standard pipeline processing, detects the X-ray sources (using WAVDETECT (Freeman et al. 2002) in the CIAO 3.2 software package¹) and determines counts in the soft (0.3–2.5 keV), hard (2.5–8.0 keV) and broad (0.3–8.0 keV) bands. A false-positive threshold of 10^{-6} in WAVDETECT is used to accept a source, corresponding to ~ 1 spurious source per ACIS-I chip, or 4 per field. The background and exposure-corrected count-rates for each source were converted to fluxes using conversion factors computed using XSPEC and assuming a power-law model ($F(E) \propto E^{-(\Gamma-1)} e^{-\sigma(E) \cdot N_{\text{H}}}$, where E is

the energy, $F(E)$ the flux density, $\sigma(E)$ is the photo-electric cross-section (Morrison & McCammon 1983), Γ is the photon index, and N_{H} is the column density associated with the absorbing material) with $\Gamma=1.7$ and $N_{\text{H}}=6 \times 10^{19} \text{ cm}^{-2}$. The analysis of the X-ray data and details on the observations will be presented in a future publication.

A total of 812 sources were detected in the initial analysis. The X-ray source list was cross-correlated with the *Spitzer* source list using a search radius corresponding to the quadratic sum of the *Chandra* positional uncertainty (2'' minimum) and of the IR positional uncertainty that was fixed to 2''. Based on the visual inspection of the images and on the low detection reliability, 20 sources are considered to be spurious. This is roughly the number expected since 1 source per ACIS chip would lead to 27 spurious sources. These X-ray sources were not included in the X-ray catalog for further analysis, reducing the total number of X-ray sources to 792. An IR counterpart is matched to 766 sources, 631 of which are also detected in the optical images. Sixteen sources are detected only in the optical and 10 X-ray sources do not have either an IR or optical counterpart. The majority of the X-ray sources (561 out of 792 sources or 71%) has a unique optical or IR counterpart within the positional uncertainty and 213 sources have multiple matches (130 sources have 2 matches, 49 have 3 matches and the remaining 34 have more than 3 matches). In the case of multiple matches the closest source was chosen as the counterpart, unless there was another candidate at similar distance that was a brighter and redder IR source (10 cases). To estimate the reality of the associations we calculated the probability of random matches between the X-ray sources and the possible *Spitzer* counterparts following the same procedure discussed in Fadda et al. (2002) and in Franceschini et al. (2005) which assumes that the IR population follows a Poisson spatial distribution. Most of the *Chandra* sources with multiple associations are unambiguously identified as the X-ray positional uncertainty is small ($\sim 2''$) and one counterpart is at less than 0.5'' from the X-ray source and the others are at more 2''. In eight cases, the positional uncertainties were so large, i.e. sources at large off-axis angles, to have several possible matches. The closest

¹*Chandra* Interactive Analysis of Observations (CIAO), <http://cxc.harvard.edu/ciao/>

source was selected, however the reliability of these matches is very low. Approximately 88% have a probability of random matches $P < 5\%$. Summing the probabilities we expect about 19 false associations in the 774 matched sources. Eighteen of the 774 matched sources are close to bright sources, mostly stars, and, therefore, do not have reliable optical and IR photometric measurements.

2.3. Radio Imaging

A deep, 1.4 GHz radio map centered at $\alpha=10^h46^m$, $\delta=+59^\circ01'$, and covering $40'\times40'$ in the *Chandra*/SWIRE field, was obtained at the Very Large Array (VLA) during multiple dates, on 2001, December 15, on 2002, January–March and on 2003, January 6 (Owen, F. et al., in preparation). VLA configurations A/B/C and D were used. The total integration time spent on source was 500 ks. The root-mean-squared (rms) noise in the center of the radio image is $2.7\,\mu\text{Jy}$. The source density decreases at larger distances from the center of the field, from about 9400 sources deg^{-2} within $10'$ from the center ($\sim 4.5\,\mu\text{Jy}$ rms), to about 4300 sources deg^{-2} at a distance between $10'$ and $20'$, and less than 1000 sources deg^{-2} at a distance greater than $20'$ ($\sim 16\,\mu\text{Jy}$ rms). There are 2052 radio sources in the entire field and 2000 are also detected in the IR with IRAC. The fraction of IR sources that are detected at radio wavelengths varies from 13% within $10'$ from the center of the radio field to about 7% in the entire radio field. The fraction of X-ray sources that are radio detected is almost four times higher than the fraction of radio detected IR sources, with 50% of all X-ray sources within $10'$ from the center and 27% in the whole field.

2.4. Optical Spectroscopy

Spectroscopic observations were carried out using various facilities, with Hydra on the WIYN Observatory on 2004, February 11–15; with the Low Resolution Imaging Spectrometer (LIRS) (Oke et al. 1995) on the Keck I telescope on February 24–25, 2004 and March 3–4, 2005; and with the Gemini Multi-Object Spectrograph (GMOS) on the Gemini Observatory on February 21–23, 2004. Details on these observations will be published in a future publication (Smith, H. et al., in preparation). Details on the Keck observations are given in section 4.1. Spectroscopic redshifts from the

Sloan Digital Sky Survey² (SDSS) are also available. In total, spectroscopic redshifts are available for 574 IR sources of which 74 are also X-ray sources, 48 from Keck, 81 from Gemini, 412 from WIYN, and 35 from SDSS.

The IR, X-ray and radio source lists and the matched multi-wavelength catalogs will be presented in a future publications (Polletta, M. et al.; Owen, F. et al., in preparation).

3. Selection of obscured AGN candidates

In the following sections, we present two methods for selecting AGN with extreme column densities ($N_{\text{H}} \gtrsim 10^{24}\,\text{cm}^{-2}$), the so called Compton-thick AGN, one based on the X-ray properties and one based on the optical-IR properties. Since the methods require knowing the redshift, and spectroscopic redshifts are available for only a small fraction of sources, we supplement the spectroscopic redshifts with photometric redshifts. Photometric redshifts were derived using the code HYPERZ (Bolzonella et al. 2000). HYPERZ measures photometric redshifts by finding the best-fit, defined by the χ^2 -statistic, to the observed SED with a library of galaxy templates. We use 24 galaxy templates that represent normal galaxies (9), starbursts (3) and AGN (12) and cover the wavelength range from 1000\AA to $500\mu\text{m}$ (Polletta et al., in preparation). The same method and template library has been used to fit the SEDs of a sample of X-ray detected AGN in the ELAIS-N1 field (Franceschini et al. 2005).

3.1. X-ray selected Compton-thick AGN

Compton-thick AGN can show a variety of X-ray spectra, soft and hard, according to the amount of absorption and reflection components (Smith & Done 1996; Matt et al. 2000). Therefore, soft X-ray spectra do not necessarily imply low or lack of absorption. However, hard X-ray spectra and X-ray luminosities greater than $10^{42}\,\text{ergs}\,\text{s}^{-1}$ can be only explained by presence of absorption and can, therefore, be used to identify obscured AGN.

In this work, we select sources with hard X-ray spectra and estimated column densities of the order of $10^{24}\,\text{cm}^{-2}$. This method is biased against

²<http://www.sdss.org>

Compton-thick AGN in which the primary radiation is completely obscured at the observed energies (<8 keV) and only the warm scattered component is observed which produces soft X-ray spectra. This selection effect is less important for high- z sources where the observed radiation is emitted at higher energies in the source rest-frame, which are less affected by obscuration, e.g.; for a column density of 10^{24} cm $^{-2}$ the observed flux between 0.3 and 8 keV is reduced by about 98% at $z \sim 0$, and by 71% at $z=2$ assuming a photon index $\Gamma=1.7$. Since most of the X-ray sources in the sample are too faint (75% of the sample has less than 50 broad-band X-ray counts) to perform full spectral fitting, the amount of absorption is estimated by comparing the counts in the hard- and soft-X-ray bands. Previous studies (Dwelly et al. 2005; Mainieri et al. 2002; Della Ceca et al. 2004; Perola et al. 2004) have shown that colour based analysis are effective in deriving the properties of X-ray sources with few counts.

Hardness ratios, HR, defined as $(H-S)/(H+S)$, where H corresponds to the X-ray counts in the hard band (2.5-8 keV) and S to the X-ray counts in the soft band (0.3-2.5 keV) were derived from the observed counts for all of the sources. In order to derive the corresponding absorption, Sherpa (Freeman et al. 2001) simulations were performed for each source assuming an absorbed power-law model. The power-law slope was fixed to a conservative (in terms of N_H estimate) $\Gamma = 1.7$ value, corresponding to the observed mean for AGN (Nandra & Pounds 1994) and the column density varied from $N_H = 10^{19}$ cm $^{-2}$ to $10^{24.5}$ cm $^{-2}$. The Bayesian method (van Dyk et al. 2004) was applied to take into account the differences in effective area across the detector by estimating the local background for each source. Each spectrum was used as input to MARX³ to create a simulated data set. Hardness ratios were calculated from the simulations of each source and the corresponding N_H were tabulated. The tabulated values were then used to determine the N_H by comparison with the observed HR. In order to derive the effective hydrogen column density, N_H^{rest} , the measured N_H was corrected for the redshift of the source taking into account the energy dependence of the photo-

electric cross section (Morrison & McCammon 1983), $N_H^{rest} = N_H^{obs} \times (1+z)^{2.6}$ (Barger et al. 2002; Longair et al. 1992). Photometric redshifts were used when spectroscopic redshifts were not available.

We found 10 X-ray sources with an intrinsic $N_H^{rest} \gtrsim 10^{24}$ cm $^{-2}$ as derived from the observed HR, assuming spectroscopic redshifts when available and photometric redshifts for the others. Photometric redshifts are still preliminary as more spectroscopic redshifts are being collected and improvements are being implemented. Currently, the total *rms* for the whole sample of 574 sources with spectroscopic redshifts is 0.26 in $1+z$, the rate of outliers (defined by $|z_{phot} - z_{spec}|/(1+z_{spec}) \geq 0.2$) is 8%, and the *rms* obtained after removing the outliers is 0.08. Although these values are consistent with those derived in other samples of galaxies and AGN (Babbedge 2004b), the uncertainties are still quite large. Therefore, after the selection based on the best photometric redshift, we examined all of the possible solutions obtained by fitting the observed SED with various templates and redshifts. After comparing the reduced χ^2_ν of all solutions with the χ^2_ν given by the best-fit solution, $\chi^2_\nu(Best)$, we removed four sources with secondary solutions with $\chi^2_\nu < 2 \times \chi^2_\nu(Best)$ at a redshift below the value required to have an $N_H^{rest} = 10^{24}$ cm $^{-2}$. Another source was removed because of poor optical and IR photometric data due to a bright nearby star which did not allow a reliable fit. The final X-ray selected sample of obscured AGN candidates contains 5 sources. Their basic properties (coordinates, r' band magnitudes, IR and radio fluxes) are reported in Table 2, their X-ray properties (broad-, soft- and hard-band X-ray fluxes, redshifts, column densities and absorption corrected broad band luminosities) are listed in Table 3, and their SEDs are shown in Figure 1.

Two sources show SEDs dominated by AGN emission. Spectroscopic data are also available for these two sources and show narrow emission lines typical of type 2 AGN. A detailed analysis of the SEDs of these two sources is presented in Sections 4, and 5. The SEDs of the other three sources are dominated by starlight in the optical and near-IR and are best-fitted with spiral galaxy templates. The estimated redshifts range from 1.4 to 2.5, the column densities range from 1.0 to 9×10^{24} and the absorption-corrected X-ray (0.3-

³<http://space.mit.edu/CXC/MARX>

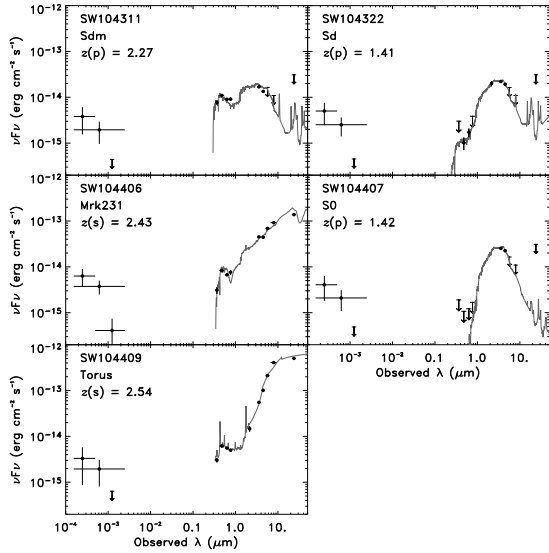


Fig. 1.— SED in νF_ν of the 5 X-ray selected Compton-thick AGN (full circles). Abbreviated source names are reported on the upper-left corner of each panel. Downward arrows indicate 5σ upper limits. The broad-, hard-, and soft-X-ray fluxes are shown as crosses. The X-ray flux energy range is indicated by the length of the horizontal line. The X-ray fluxes are derived assuming an absorbed power-law model with photon index, Γ equal to 1.7 and Galactic absorption, $N_H = 6 \times 10^{19} \text{ cm}^{-2}$. A downward arrow at 2σ limit is used in the X-rays when the counts are less than 1σ . The best-fit template for each object is shown as a grey curve and the template name is reported in each panel. The spectroscopic ($z(s)$) or photometric ($z(p)$) redshift of each object is also reported.

8 keV) luminosities from 2.5×10^{45} to 9.5×10^{45} ergs s^{-1} implying that these are all Compton-thick quasars.

3.2. IR-selected obscured AGN

Since Compton-thick AGN might be too faint in the X-rays to be detected at our sensitivity level, we need a complementary selection method that can be applied to the entire IR sample independently of their X-ray data.

In obscured AGN, the X-ray radiation is absorbed by gas and dust surrounding the nuclear region and re-emitted in the mid- and far-IR after being thermally reprocessed. Since IR radiation is less affected by obscuration than optical and X-ray emission, AGN selection at these wavelengths is less biased against obscured AGN. However, AGN usually represent only a small fraction of all of

the sources detected in IR surveys compared to the far more numerous and strong IR emitters, such as galactic sources, normal and starburst galaxies. Moreover, their IR spectral properties can be indistinguishable from those of non AGN sources when only a few IR bands are available. IR-selected AGN can thus be less reliable than X-ray and optical selected samples. The *Spitzer Space Telescope* (Werner et al. 2004), thanks to the wavelength range accessible to IRAC (Fazio et al. 2004), offers the capability to easily identify a large fraction of the AGN population (Lacy et al. 2004; Stern et al. 2004) through a simple color analysis that efficiently removes the majority of non-AGN sources.

In the mid-IR, AGN are characterized by red and almost featureless spectra (Houck et al. 2005; Hao et al. 2005; Weedman et al. 2005). These properties make their IRAC (3.6, 4.5, 5.8, and 8.0 μm) colors unique among other IR sources, such as galaxies and stars, providing a powerful tool to identify them (Lacy et al. 2004; Stern et al. 2004; Hatziminaoglou et al. 2005). However, this diagnostic is effective only when the AGN is the dominant energy source. In cases where thermal radiation produced by dust associated with the AGN is self-absorbed and/or thermal radiation from dust in star-forming regions is more luminous than that produced by the AGN, e.g. as in the Seyfert 2 galaxies NGC 4945 and NGC 6240 (Maiolino et al. 2003; Rigopoulou et al. 1999), the AGN IR emission is fainter or negligible compared to that produced by star-formation processes in the host-galaxy (Peeters et al. 2004). The IR SED and IRAC colors of these AGN may be indistinguishable from those of starburst and normal star-forming galaxies (i.e. dominated by cool/warm dust and PAH features at $z < 0.6$ and by stellar light at $z > 0.6$) (Franceschini et al. 2005; Alonso-Herrero et al. 2004; Rigby et al. 2004). In these sources, the AGN might manifest itself at other wavelengths, in the X-rays, if not completely obscured, as in the 3 stellar-dominated Compton-thick X-ray AGN reported in Section 3.1, in the radio or in optical and IR spectra, if the light is not diluted by the host galaxy starlight (Moran, Filippenko, & Chornock 2002).

In order to select heavily obscured AGN candidates among the IR population independently of their X-ray properties, we require a red and

featureless IR SED, and red optical SEDs or red optical-IR colors to remove unobscured AGN. This requirement would be satisfied by only a subset of all obscured AGN for the reasons given above. We first selected all of the extragalactic IR sources that are detected at a 5σ level in at least 3 IR bands over the wavelength range 3.6-24 μm . This reduced the IR sample from 41,262 to 4493 sources of which 2726 (60%) are detected at 24 μm . Note that about 46% of the extragalactic X-ray sources with an IR counterpart in the SWIRE/*Chandra* field do not satisfy this selection criterion. The next step in the selection procedure is done automatically through an algorithm that calculates the spectral slope and goodness of a power-law model fit to the observed SED (νF_ν) between 2.15 and 24 μm , which includes the K_s -band data, the four IRAC bands and the MIPS 24 μm band. All of the sources with a monotonically rising IR SED, a spectral slope α_{IR} (defined as $F_\nu \propto \lambda^{\alpha_{IR}}$) larger than 1.0 and reduced $\chi^2_\nu < 13.3(\alpha_{IR} - 1) \leq 20$ are then selected. The slope threshold is defined to reject sources with blue SEDs typical of early-type galaxies. The χ^2 -test is used to select sources with smooth red SEDs, not necessarily power-law like, and to remove sources with variations in their SEDs due to the presence of spectral features, e.g. PAHs. AGN may show IR SEDs with a convex round shape in $\text{Log}(F_\nu)$ instead of a straight power-law spectrum, or a dip at 24 μm due to the 9.7 μm Silicate absorption feature at $z \sim 1.5$ (Franceschini et al. 2005; Alonso-Herrero et al. 2004; Rigby et al. 2004; Rigby et al. 2005; Houck et al. 2005; Weedman et al. 2005; Hao et al. 2005). For these AGN a power-law model fit does not provide a good fit, but it is a reasonable first-order approximation to their IR SEDs. The expected α_{IR} and χ^2_ν values for AGN and normal galaxies were derived from a simulated catalog of sources of different types and redshifts and several combinations of detections in the same filter systems as available for the SWIRE catalog. The simulated catalog was created from the same template library used to derive photometric redshifts and uncertainties to the observed fluxes were added in order to resemble those of the SWIRE catalog. The SEDs of a sub-set of randomly selected objects with a broad range of χ^2 and α_{IR} were also visually inspected for verification and parameters tuning. Non-detections were taken into

account by requiring the power-law model to be consistent with the upper limits. This selection reduces the sample from 4493 to 248 sources of which 93% are detected at 24 μm . Although the selection does not require a detection at 24 μm , the large fraction of 24 μm sources is not surprising due to the combination of the minimum required power-law slope ($\alpha_{IR}=1$) and the SWIRE sensitivity. The faintest source with $\alpha_{IR}=1$ and detected in 3 IRAC bands will have a 24 μm flux of 120 μJy , only a factor of 2 lower than our 5σ limit. Sources with brighter fluxes and redder SED will then be easily detected at 24 μm . Only 23% (90 sources) of the X-ray detected sources with 3 IR detections have IR SEDs that satisfy the above criterion. This is consistent with previous SED analysis of X-ray selected AGN which find typical AGN SEDs for only $\sim 30\%$ of all X-ray selected AGN (Franceschini et al. 2005). In order to remove likely unobscured quasars, we then selected all of the sources with optical-IR colors redder than those typical of unobscured quasars or red optical SEDs. These requirements are satisfied if a power-law ($F_\nu \propto \lambda^{\alpha_{opt}}$) fit to the optical SED of a source detected in g' , r' , i' has a slope, α_{opt} , greater than 2, or if at least two of the following conditions are verified, $F(3.6\mu\text{m})/F(g') \geq 15$, $F(3.6\mu\text{m})/F(r') \geq 13$, and $F(3.6\mu\text{m})/F(i') \geq 10$. This final criterion is satisfied by 181 sources, of which 78 do not have an optical counterpart at the survey limits (see Section 2.1). Note that for blank sources fainter than 16 μJy at 3.6 μm and located where the optical observations are the least sensitive ($\delta < 58.6^\circ$) this criterion can not be verified, but at this stage of the selection, they are kept in the sample for completeness. This selection removes 67 sources, of which 42 are X-ray sources. Among the rejected sample, 61 sources have optical-IR SEDs consistent with those of unobscured AGN like optically selected quasars.

The SEDs of the remaining 181 obscured AGN candidates were fitted using HYPERZ and the library of 12 normal galaxy and 12 AGN templates. Only the sources that did not have any acceptable solutions (a minimum in the χ^2_ν distribution) with normal galaxy templates were kept for a final sample of 120 sources. Among the rejected sources, several can be high redshift galaxies whose optical and near-IR emission is due to stellar light. Some of the rejected sources might host an AGN,

but in order to increase our sample reliability we decided to remove any dubious cases. This selection removes 7 X-ray sources from the sample, yielding a total of 41 X-ray sources among the IR-selected obscured AGN. The X-ray properties of the 41 X-ray sources out of the 120 IR-selected sample of AGN candidates are reported in Table 5 and described in Section 3.2.1. For all of the selected sources, even for those that are not detected in the optical images, the $3.6\mu\text{m}$ over optical flux ratio is constrained to be higher than the limits given above. The IRAC colors of the selected sample compared to the rest of IR sources in the *Chandra*/SWIRE field are shown in Figure 2. The dashed line delimits the region where AGN are most likely to be found (Lacy et al. 2004) (see also Stern et al. (2004); Hatziminaoglou et al. (2005)).

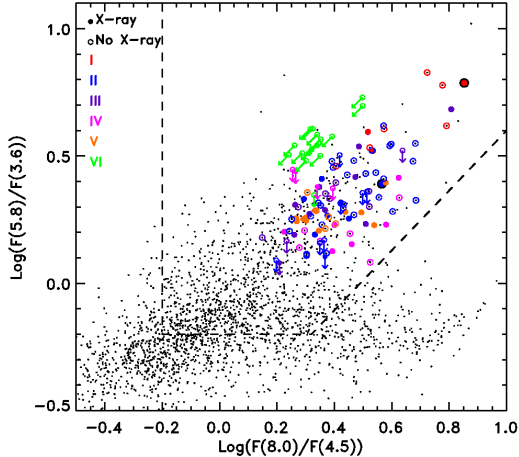


Fig. 2.— IRAC color-color diagram ($F(5.8\mu\text{m})/F(3.6\mu\text{m})$) versus $F(8.0\mu\text{m})/F(4.5\mu\text{m})$) of all of the IR sources detected in four IRAC bands in the *Chandra*/SWIRE field (black dots). IR-selected obscured AGN candidates are shown as open circles, or full circles if they are also X-ray sources. Downward arrows indicate sources that are not detected at $5.8\mu\text{m}$, and arrows pointing toward the bottom-left corner indicate sources that are not detected at neither $5.8\mu\text{m}$ nor $8.0\mu\text{m}$. The colors correspond to different SED types (I:red, II:blue, III:purple, IV:magenta, V:orange and VI:green) (see Section 3.2). The two confirmed Compton-thick quasars, SW104406 and SW104409, are shown with large black circles (see section 5). The dashed line shows the region preferentially occupied by AGN, identified by Lacy et al. (2004).

In the initial sample of 4493 sources, less than 9% are X-ray sources, but 34% of the selected sam-

ple of obscured AGN candidates are X-ray sources. Among the IR-selected AGN that were rejected because consistent with unobscured AGN, 63% are X-ray sources. These values are consistent with a selection that favors AGN. Only two sources are not detected at $24\mu\text{m}$ and four have a $24\mu\text{m}$ flux below the nominal 5σ limit. A $24\mu\text{m}$ detection for these four sources was confirmed after a visual inspections of the images. Note that the sensitivity of the $24\mu\text{m}$ data varies across the field due to a variation in the number of coverages. The adopted 5σ limit of $230\mu\text{Jy}$ is valid for the areas with median coverage in the SWIRE/*Chandra* field.

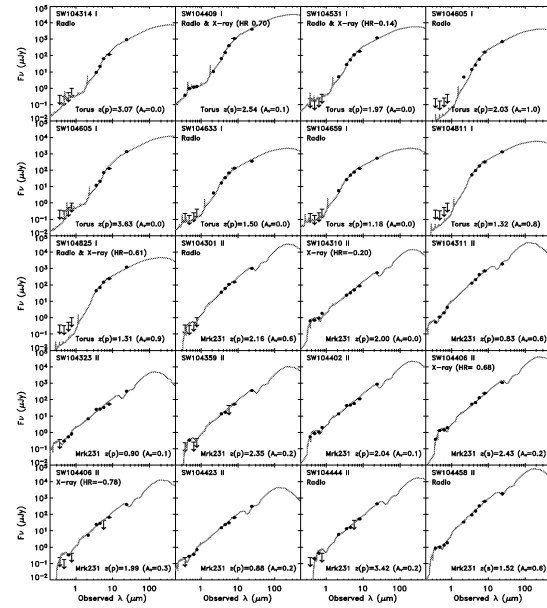


Fig. 3.— SEDs of the 120 IR-selected obscured AGN candidates. Five σ upper limits are reported as downward arrows. The sources are ordered by SED class, from I to VI (see text) and by right ascension within each SED class. The abbreviated source name and the SED class are given on the upper-left corner of each panel. Each SED class is fitted with an AGN template (I: Torus, II: Mrk 231, III: QSO1, IV: IRAS 19254–7245 South, V: QSO2, and VI with any of the previous templates). The best-fit template for each source at the spectroscopic redshift, $z(s)$, if available, or at the photometric redshift, $z(p)$, is shown as a grey curve. The amount of extinction applied to the template and the redshift are reported on the bottom-right corner in each panel. X-ray sources are identified by the note “X-ray” on the upper-left corner and the HR value is also given and radio sources are identified by the note “Radio”.

The sample was divided in six categories, from I to VI, five categories (I–V) were defined based

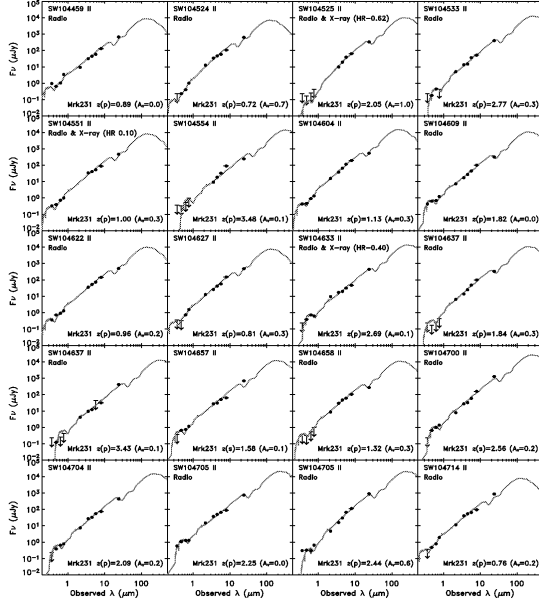


Fig. 3.— *Continued*

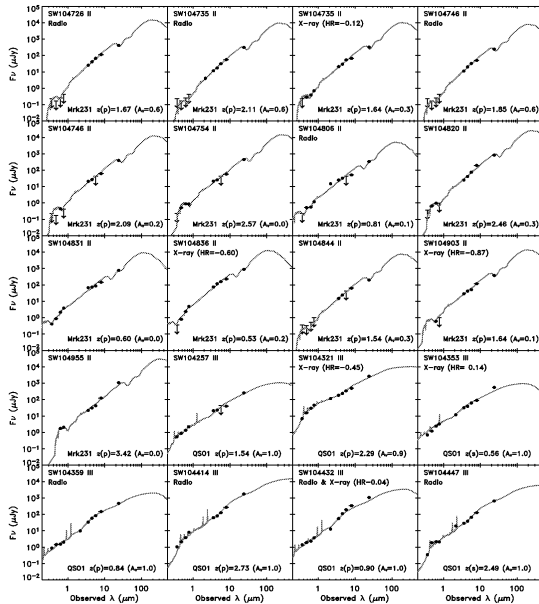


Fig. 3.— *Continued*

on their best-fit template one category (VI) was defined based on the low number (3) of detections in the IR. Class I sources (9) have IR SEDs characterized by a convex shape that are well fitted with a “Torus” template (see Section 5.1). Class II

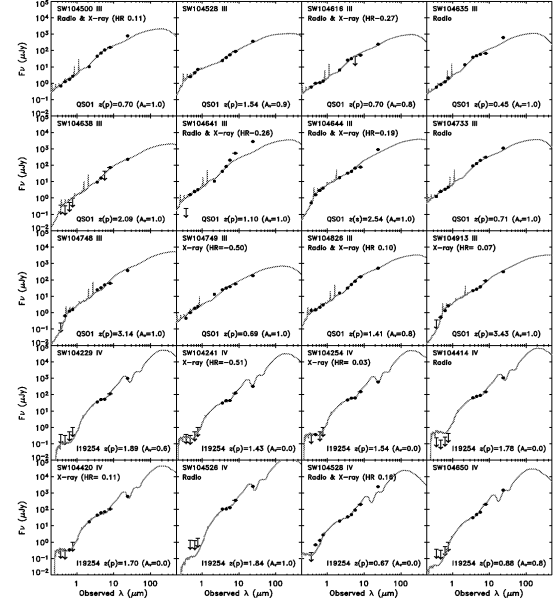


Fig. 3.— *Continued*

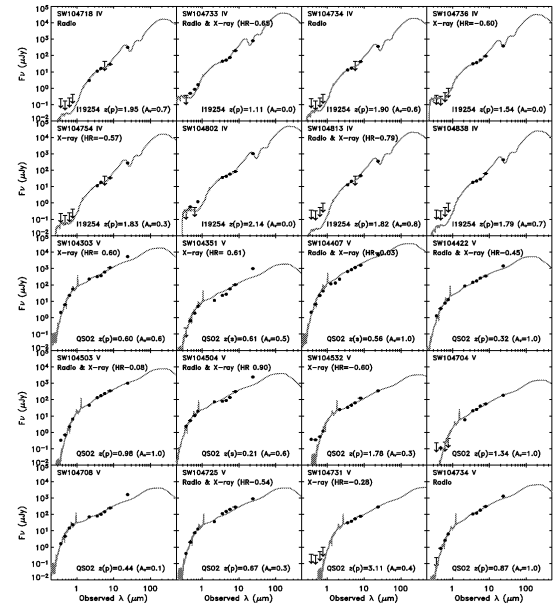


Fig. 3.— *Continued*

sources (44) show power-law like optical-IR SEDs, similar to Mrk 231 or slightly redder ($A_V < 1$). Similarly, class III sources (19) have power-law like optical-IR SEDs, but not as red as Mrk 231; a reddened QSO template ($A_V = 0.6-1.0$) provides a

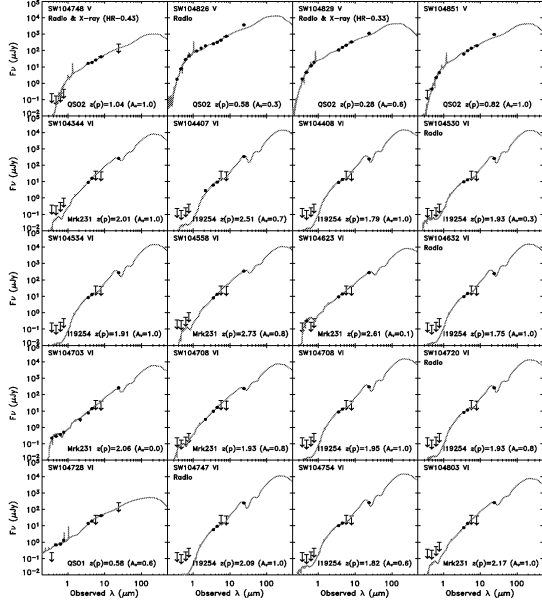


Fig. 3.— *Continued*

better fit. Class IV sources (16) show SEDs consistent with templates of composite sources with contributions from both star-forming regions and an AGN component. This interpretation is supported by an excess at $24\mu\text{m}$ with the respect to the extrapolation of the power-law representing the hot dust continuum associated with the AGN, this excess is likely associated to emission from the PAH bands. Class V objects (16) are characterized by a turnover in the SED with optical SEDs much redder than the IR SED. These sources might be composite objects where the optical emission is dominated by stellar light, from either an old or a reddened stellar population, and the IR emission is associated to the AGN. Class VI objects (16) are fainter than the rest of the sample and detected only in three bands from 3.6 to $24\mu\text{m}$, their SEDs show a distinct signature of AGN in their extreme red $F(4.5\mu\text{m})/F(3.6\mu\text{m})$ flux ratios. Upper limits to the flux in the bands are consistent with the models used to describe the other classes. Names, coordinates, r' magnitudes, IR fluxes and classification of the IR-selected obscured AGN candidates are listed in Table 4 and their SEDs are shown in Figure 3. Photometric redshifts were used to over-plot the best-fit template on each SED when spectroscopic redshifts

were not available. The redshifts are used only to visually characterize the SED shape of these sources by comparing them with AGN templates.

Only eleven sources have spectroscopic redshifts. Spectroscopic redshifts are indicated as $z(s)$ and photometric redshifts as $z(p)$ in Figure 3 and listed in Table 4. The optical spectra of seven sources (SW104351, $z=0.609$; SW104409, $z=2.540$; SW104406, $z=2.430$; SW104447, $z=2.488$; SW104644, $z=2.542$; SW104657, $z=1.579$; and SW104700, $z=2.562$), show emission lines from an AGN, e.g. Ly α , C IV $\lambda 1549$, and their width ranges from 1200 to ~ 1700 km/s, typical of narrow-line or type 2 AGN. The optical spectrum of SW104407 ($z=0.555$) is dominated by stellar light typical of a post-starburst galaxy (Balmer absorption line) and high-ionization narrow emission lines, [Ne V] $\lambda 3426$, [Ne III] $\lambda 3869$, from the AGN. Two sources, SW104353 ($z=0.563$) and SW104458 ($z=1.52$), show only one emission line, [O II] $\lambda 3727$, consistent with emission from newborn stars. No AGN signatures are observed, but the optical spectra are characterized by low signal-to-noise. The spectrum of SW104504 ($z=0.214$) shows broad Balmer emission lines, H α , H β , and the [O III] $\lambda 5007$ forbidden line, typical of a starburst galaxy.

3.2.1. X-ray properties of the IR-selected obscured AGN candidates

A small fraction, 41 sources, corresponding to 34% of the IR-selected obscured AGN candidates are also X-ray detected. Five of these 41 X-ray sources have multiple IR counterparts. However, in all five cases the matched source is at less than $1''$ from the X-ray source with a probability of random association $<1.3\%$, and the neighbour sources are more than $2''$ distant. Therefore, we consider all these associations reliable. The 41 X-ray sources show all types of optical-IR SEDs, except class VI. Their X-ray spectra (see Table 5) show a wide range of hardness ratios, from -0.87 to 0.90 , with a median value of -0.26 . Assuming our redshift estimates to derive the intrinsic column density and a photon index $\Gamma=1.7$, 26 (63%) sources have column densities larger than 10^{22} cm^{-2} and of these, 12 have $N_{\text{H}}>10^{23}$ cm^{-2} . Only two sources are also present in the X-ray selected sample of Compton-thick ($N_{\text{H}}>10^{24}$ cm^{-2}) AGN, SWIRE_J104409.95+585224.8 (SW104409 here-

after) and SWIRE_J104406.30+583954.1 (SW104406 hereafter).

3.2.2. Optical versus X-ray flux

The optical and broad-band (0.3-8 keV) X-ray fluxes of all of the X-ray sources in the *Chandra*/SWIRE field and of the IR-selected obscured AGN candidates are compared in the top panel of Figure 4 where the X-ray sample is shown as black open circles and the IR-selected sample as full circles. We use the full band flux to minimize the uncertainty associated with the factors used to convert counts to flux. The distribution of r' -band fluxes for the IR-selected sample is shown in the bottom panel of Figure 4. The sample of IR-selected obscured AGN candidates is shown as full circles of different colors according to their classification (I in red, II in blue, III in purple, IV in magenta, V in orange and VI in green). The X-ray-selected sources are shown as cyan full circles. In case of no optical detection a left pointing arrow at the 5σ r' -band value is shown and in case of no X-ray detection a downward arrow at 10^{-15} $\text{ergs cm}^{-2} \text{s}^{-1}$ is shown. We also plot the expected observed fluxes of four AGN templates at various redshifts from 0.1 to 3. The AGN templates correspond to the median of a sample of optically selected quasars (Elvis et al. 1994): “Elvis QSO”, the Compton-thick BAL QSO/Seyfert 1 galaxy Mrk 231 ($z=0.042$; Braito et al. (2004)), and the Compton-thick Seyfert 2 galaxies IRAS 19254–7245 South (I19254) ($z=0.0617$; Berta et al. (2003); Braito et al. (2003)) and NGC 6240 (N6240) ($z=0.0244$; Vignati et al. (1999); Iwasawa et al. (2001)). All templates other then the “Elvis QSO” are characterized by extreme (Compton-thick) absorption in the X-rays. The hatched area represents the locus of $F(X)/\nu F(r')$ between 0.1 and 10, which is traditionally considered the locus where “classical” AGN lie (Akiyama et al. 2003). Sources with $F(X)/\nu F(r') > 10$ are expected to be mostly obscured AGN at high- z (Perola et al. 2004), while sources with $F(X)/\nu F(r') < 0.1$ are expected to be mostly star-forming galaxies whose X-ray emission is not powered by an AGN. However, this simple picture becomes more complex for fainter AGN (Comastri et al. 2003).

The three Compton-thick AGN templates are characterized by low X-ray over optical flux ratios ($F(X)/\nu F(r') < 0.1$) at low- z and as the

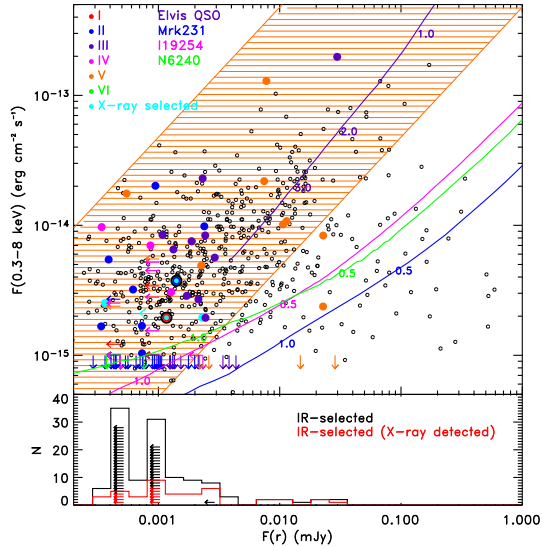


Fig. 4.— Top panel: Broad (0.3-8 keV) X-ray flux versus the r' -band flux of all of the X-ray sources in the *Chandra*/SWIRE field (black open symbols), of X-ray selected obscured AGN candidates (cyan) and of IR-selected obscured AGN candidates (I:red, II:blue, III:purple, IV:magenta, V:orange and VI:green). Downward arrows represent sources not detected in the X-rays and leftward arrows represent sources not detected in the optical r' -band. The X-ray fluxes are derived assuming an absorbed power-law model with photon index, Γ equal to 1.7 and Galactic absorption, $N_{\text{H}}=6\times 10^{19} \text{ cm}^{-2}$. The two Compton-thick quasars, SW104406 and SW104409, are shown with large black circles. The orange shaded area delimits the region of $\text{Log}(F(X)/\nu F(r')) = \pm 1$, typical of “classical” AGN. The purple, blue, magenta and green curves represent the tracks of known AGN at various redshifts as annotated, the Elvis QSO template (purple), Mrk 231 (blue), IRAS 19254–7245 South (magenta) and NGC6240 (green). Bottom panel: Distribution of the r' -band flux of the IR-selected sample of obscured AGN candidates. The black line represents the entire IR-selected sample, the red curves shows only the X-ray detected subsample. Left-pointing arrows represent r' -band 5σ upper limits, each arrows refers to a single source.

redshift increases, they move into the locus of “classical” AGN. Thus, extreme $F(X)/\nu F(r')$ ratios are not expected for local Compton-thick AGN even at high redshifts. Lower flux ratios ($F(X)/\nu F(r')=0.1-10$), consistent with those of classical AGN, are also observed in the X-ray selected Compton-thick AGN sample. The majority (108) of the IR-selected obscured AGN candidates also has $F(X)/\nu F(r')=0.1-10$, 91 of which show $F(X)/\nu F(r')$ between 0.1 and 1 and 12 sources have $F(X)/\nu F(r') < 0.1$. It is clear that obscured AGN do not have unique $F(X)/\nu F(r')$ ratios. Therefore, a selection based on large (>10)

$F(X)/\nu F(24\mu\text{m})$ values would miss a large fraction of obscured AGN.

3.2.3. Mid-Infrared versus X-ray flux

The observed mid-IR flux at $24\mu\text{m}$ and the broad-band (0.3-8 keV) X-ray flux for the X-ray sample in the *Chandra*/SWIRE field are compared in the top panel of Figure 5 where the X-ray sample is shown as black open circles. Downward arrows indicate the full band (0.3-8 keV) flux upper limit of 1×10^{-15} $\text{ergs cm}^{-2} \text{s}^{-1}$ and leftward arrows indicate the $230\mu\text{Jy}$ 5σ limit at $24\mu\text{m}$. The sample of X-ray and IR-selected obscured AGN shown in Figure 4 is also shown in Figure 5 as full circles or downward arrows in colors corresponding to different classes (from I to VI). The curves represent the expected observed fluxes of the four AGN templates shown in Figure 4 at various redshifts from 0.1 to 3. In the bottom panel of Figure 5, the distribution of $24\mu\text{m}$ fluxes of the IR-selected sample of obscured AGN candidates is shown.

Hard X-rays to mid-IR flux ratios in the local Universe range from 10^{-3} for starburst galaxies to $\simeq 1$ for unobscured AGN (Alexander et al. 2001; Manners et al. 2004; Lutz et al. 2004). The locus occupied by hard X-ray-selected AGN from the Piccinotti et al. (1982) sample with detected mid-IR emission and $z < 0.12$ corresponds to the hatched area in orange ($F(X)/(\nu_{24}F(24\mu\text{m}))=0.19-1.17$). The locus occupied by local starburst galaxies corresponds to the hatched pink area ($F(X)/(\nu_{24}F(24\mu\text{m})) = 5\times 10^{-4} - 3\times 10^{-3}$). The two loci have been adapted from Alonso-Herrero et al. (2004) after correcting the X-ray flux from 2-10 keV to 0.3-8 keV assuming an absorbed power-law model with $N_{\text{H}}=10^{21} \text{ cm}^{-2}$ and spectral index $\Gamma=1.7$ for the Piccinotti's sample and $\Gamma=2.0$ for the starbursts. Sources with low or no absorption, such as the Elvis QSO template, show large X-ray over mid-IR flux ratios which are almost constant up to $z=4$ (0.6–0.9). Sources characterized by large column-densities are characterized by a broader range of $F(X)/(\nu_{24}F(24\mu\text{m}))$ values, from 6×10^{-4} to 0.6 for $z < 4$. Their X-ray over mid-IR flux ratios increase at larger redshifts, moving them into the region occupied by unobscured AGN. As absorption increases the X-ray flux decreases, while the $24\mu\text{m}$ flux is only slightly affected. At higher- z ,

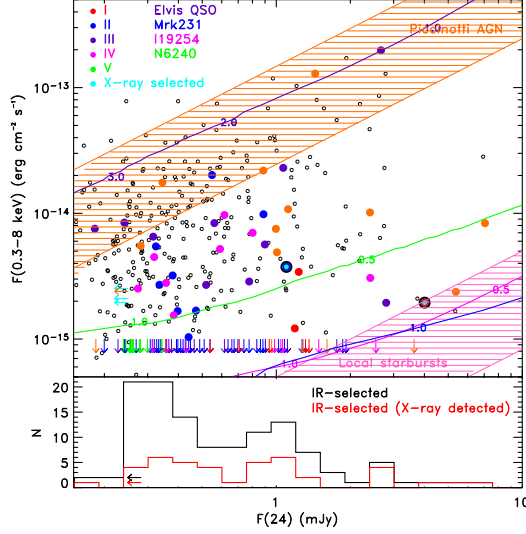


Fig. 5.— Top panel: Broad (0.3-8 keV) X-ray flux versus the $24\mu\text{m}$ flux of all of the X-ray sources in the *Chandra*/SWIRE field (black open circles). Symbols as in Figure 4. The orange dashed area represents the area that the AGN in the Piccinotti's sample (Piccinotti et al. 1982) would occupy and the pink area represents the area that local starburst galaxy would occupy (adopted from Alonso-Herrero et al. (2004)). The X-ray fluxes are derived assuming an absorbed power-law model with photon index, Γ equal to 1.7 and Galactic absorption, $N_{\text{H}}=6\times 10^{19} \text{ cm}^{-2}$. Bottom panel: Distribution of the $24\mu\text{m}$ flux of the IR-selected sample of obscured AGN candidates. The black line represents the entire IR-selected sample, the red curves refers only to the X-ray detected sub-sample. Left-pointing arrows represent $24\mu\text{m}$ 5σ upper limits.

however, the IR flux decreases more rapidly since the observed wavelengths correspond to shorter wavelengths in the rest-frame and the X-ray flux becomes less affected by obscuration as higher energy photons are collected, resulting in larger X-ray/24μm flux ratios (Alexander et al. 2001; Fadda et al. 2002; Manners et al. 2004).

All of the X-ray selected Compton-thick AGN show X-ray/mid-IR flux ratios lower than those of unobscured AGN ($F(X)/(\nu_{24}F(24\mu\text{m}))=0.001-0.03$). Among the IR-selected obscured AGN candidates only 7 sources (SW104310, SW104321, SW104422, SW104532, SW104616, SW104725, SW104749) have $F(X)/(\nu_{24}F(24\mu\text{m})) > 0.19$ as the Piccinotti's sample. Three of these 7 sources are obscured in the X-rays ($N_{\text{H}} > 10^{22} \text{ cm}^{-2}$). Thus, obscured AGN do not show unique $F(X)/(\nu_{24}F(24\mu\text{m}))$ values, however low values

(<0.2) are more likely. This results is in agreement with a recent study of X-ray and $24\mu\text{m}$ -selected AGN, which shows that there is no correlation between $F(X)/\nu_{24}F(24\mu\text{m})$ and the amount of absorption in the X-ray or their optical properties (Rigby et al. 2005).

The range of IR and optical fluxes of the X-ray detected sources are very similar to the values observed in the entire IR-selected sample of obscured AGN candidates (see bottom panels of Figures 4 and 5). However, there is a higher fraction of faint sources in the whole sample compared to the X-ray detected sub-sample, and the majority of sources has smaller X-ray over $24\mu\text{m}$ flux ratios. Smaller ratios suggest that the fraction of obscured sources and/or the amount of absorption is higher in the non X-ray detected sub-sample. Since we can not quantify the amount of obscuration in the non X-ray detected sources, we assume that the distribution of absorption in the entire IR-selected sample is similar to that observed in the X-ray detected sub-sample (63% with $\text{N}_\text{H} > 10^{22} \text{ cm}^{-2}$, 29% with $\text{N}_\text{H} > 10^{23} \text{ cm}^{-2}$, and 5% with $\text{N}_\text{H} > 10^{24} \text{ cm}^{-2}$). However, it is plausible that the estimated fractions of obscured sources are only lower limits to the real distribution for the reasons given above.

Although the ratios between the X-ray flux and the optical or the mid-IR flux are affected by absorption, they cannot be used as an effective method to select obscured AGN. As shown in the two previous sections and in previous works (Rigby et al. 2004), these flux ratios also depend on the AGN luminosity, the host galaxy contribution and redshift, and, therefore, they are not unique for AGN with large amounts of absorption.

3.2.4. Radio properties of the IR-selected obscured AGN candidates

Although a detailed discussion on the radio properties of the AGN in this field and on the radio population in general will be presented in future works, here we give a brief summary of the radio detection rate of the IR-selected obscured AGN candidates. Half (60 sources) of the sample is detected in the radio (see Table 4). The fraction of radio sources per class, I, II, III, IV, V, and VI, is, respectively, 77, 50, 57, 43, 56 and 25%. The fraction of radio sources among the IR-selected obscured AGN candidates is much higher

than the fraction of radio sources among either all IR sources or all X-ray sources. More specifically, within $12'$ from the center of the radio field, there are 26 IR-selected obscured AGN and 24 (=92%) are radio sources. The fraction of radio sources in this area per class is 100% (2/2) of class I, 92% (11/12) of class II, 100% (6/6) of class III, 100% (1/1) of class IV, 75% (3/4) of class V, and 100% (1/1) of class V. Since large ratio powers are usually associated with the presence of an AGN, the high fraction of radio detection of this sample is consistent with the hypothesis that these sources are mainly powered by an AGN.

4. Photometric and spectroscopic data of SW104409 and SW104406

Having discussed some general properties of the X-ray and IR-selected obscured AGN candidates in the SWIRE/*Chandra* field, we now focus on the only two sources that are selected by both selection methods, SW104409 and SW104406. These two sources are the only ones among the X-ray sample of Compton-thick AGN for which a spectroscopic redshift is available, providing a confirmation on their Compton-thick nature. In this section we review the available multi-wavelength data for the two sources and in the next section we construct their SEDs, compare them to those of other Compton-thick AGN and present a simple model to explain the observed properties.

Optical and IR photometric fluxes as measured during the observations described in section 2.1 for SW104409 and SW104406 are listed in Table 6 and 7.

4.1. Optical Spectroscopy

Spectroscopic observations for SW104409 and SW104406 were carried out on 2005 March 03 and 04, respectively, with the Low Resolution Imaging Spectrometer (LIRS) (Oke et al. 1995) on the Keck I telescope. The observations were taken in multi-object mode and three equal integrations were performed for a total exposure time of 1.5 hour. The observations were taken with $1''.5$ wide slitlets aligned near the parallactic angle. The effective wavelength range of the blue spectrograph of the instrument is $3500\text{--}6700\text{\AA}$. A 300 lines/mm grism with a blaze wavelength of 5000\AA was used resulting in 1.43 \AA/pixel dispersion. We used a

HgAr lamp spectrum obtained at the same position angle immediately following the observations for wavelength calibration. The night was photometric with $\sim 1''.3$ seeing and the spectra were calibrated using the observations of the standard star G191B2B from Massey et al. (1988). The spectra of SW104409 and SW104406 are shown in Figures 6 and 7, respectively. The optical flux and spectral shape of SW104409 and SW104406 at the time of the Keck observations are consistent, within 1σ , with the earlier broad-band g' and r' photometric measurements.

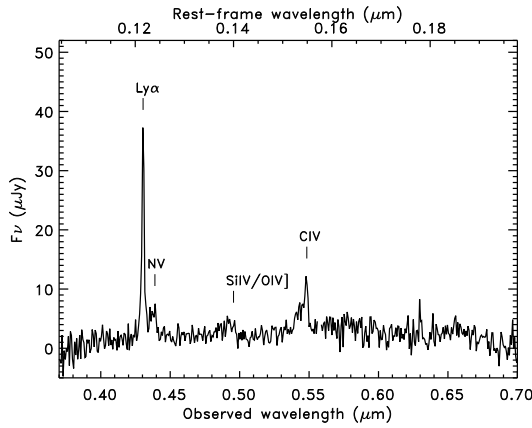


Fig. 6.— Optical spectrum of SW104409 obtained with the Keck I telescope. Detected emission features are labeled.

The spectrum of SW104409 shows a narrow ($\text{FWHM} = 1324 \pm 80 \text{ km s}^{-1}$) Ly α emission line and two asymmetric emission lines with a broad blue-ward component, C IV $\lambda 1549$ and N V $\lambda 1240$. The spectrum of SW104406 shows several narrow emission lines, e.g.; Ly α with $\text{FWHM} = 1360 \pm 20 \text{ km s}^{-1}$ and C IV $\lambda 1549$ with $\text{FWHM} = 1485 \pm 60 \text{ km s}^{-1}$. The line identifications and parameters (FWHM, fluxes and the rest-frame equivalent width ($W_{\lambda, \text{rest}}$)), calculated for single Gaussian fits using IRAF (Kriss 1994), are listed in Table 8 and 9. In the case of SW104409, since the signal-to-noise is too low to constrain a Gaussian fit for the broad component of the asymmetric emission lines, the total flux and equivalent width were derived by integrating the total spectrum around the lines and subtracting the continuum (see Table 8). The estimated mean redshifts are 2.54 ± 0.02 for SW104409, and 2.430 ± 0.003 for SW104406.

According to the properties of its optical spectrum, SW104406 is a classical type 2 QSO, while SW104409 could be considered a peculiar type 2 QSO because of the superposition of weak asymmetric broad components on top of the stronger narrow emission lines.

A more detailed analysis and an in depth investigation of the spectrum of SW104409 is beyond the scope of this work. The blue-shifted broad components of the C IV $\lambda 1549$ and N V $\lambda 1240$ emission lines suggest the presence of highly ionized gas moving toward the observer as an outflow or wind from the accretion disk as observed in other quasars (Gallagher et al. 2005). However, this interpretation is difficult to reconcile with a geometry in which the AGN is obscured.

4.2. X-ray Data and Spectral Analysis

Details (seq. N., OBSID and exposure time) on the X-ray observations of SW104409 and SW104406 are listed in Table 10. SW104409, located at an off-axis angle of $3''.6$ has 11 broad-band counts, only 2 of which fall in the soft band. SW104406, at an off-axis angle of $5''.8$, is brighter in the X-ray than SW104409 with 22 broad-band counts and 3 in the soft band. With so few counts, the error on the source's hardness ratio is large and spectral modeling would not constrain any parameter. Therefore, in order to constrain the amount of absorption in these sources we applied the Bayesian method described in section 2.2 (van Dyk et al. 2004). We derive an HR of $0.85^{+0.06}_{-0.39}$ for SW104409 and of $0.61^{+0.21}_{-0.23}$ for SW104406, which correspond to intrinsic column densities of $2.0^{+0.5}_{-1.3} \times 10^{24} \text{ cm}^{-2}$ for SW104409 and $1.0^{+0.7}_{-0.3} \times 10^{24} \text{ cm}^{-2}$ for SW104406. These extreme column densities indicate that both sources are borderline Compton-thick AGN. Alternative models, such as a reflection component due to ionized or neutral gas, can not be ruled out, but they would also indicate large column densities ($\sim 10^{24} \text{ cm}^{-2}$). Assuming that the X-ray spectra of SW104409 and SW104406 are due to transmitted components through column densities of $N_{\text{H}} = 2 \times 10^{24} \text{ cm}^{-2}$, and $N_{\text{H}} = 1 \times 10^{24} \text{ cm}^{-2}$, respectively, then the absorption-corrected X-ray luminosities in the rest-frame, assuming a photon index $\Gamma = 1.7$, are $4 \times 10^{45} \text{ ergs s}^{-1}$ and $5 \times 10^{45} \text{ ergs s}^{-1}$, respectively.

4.3. Radio Data

SW104409, located at $17'$ from the center of the radio field, is unresolved, but clearly detected. Its radio flux, measured on an image convolved to $3''$ to reduce instrumental effects this far off-axis, is $273 \pm 15 \mu\text{Jy}$. SW104406, located at the edge of the radio field ($26'$ off-axis), is not detected in the radio (there is only an apparent 2.4σ detection), therefore we assume a 3σ upper limit to its radio flux of $162 \mu\text{Jy}$.

5. Spectral Energy Distributions of SW104409 and SW104406

In this section, we analyze the spectral energy distributions (SEDs) from X-ray to radio wavelengths of the two obscured quasars discussed above, SW104409 and SW104406. The SED shapes and luminosities are compared to those of known AGN: Elvis QSO template and the BAL QSO/Seyfert 1 galaxy Mrk 231. The SEDs are interpreted assuming the unification scenario for which the absorbing material is distributed around the central source in a toroidal shape. However, alternative models can not be ruled out by the available data.

5.1. SW104409

The SED of SW104409, from X-ray to radio wavelengths, is shown in Figure 8 and compared to the SED of Mrk 231. SW104409 is characterized by a blue optical spectrum up to 2200\AA in the source rest-frame, followed by a rapid rise at longer wavelengths with an observed $r' - K_s = 4.13$ (Vega), fitting the conventional definition of extremely red object (ERO; $R - K > 4$) (Elston et al. 1988). The U-band drop-out is probably due to intergalactic medium (IGM) attenuation (Madau 1995), as expected for such a high redshift object. The comparison with Mrk 231 shows how extreme the IR SED of SW104409 is ($F^{\text{rest}}\nu(2.2\mu\text{m})/F^{\text{rest}}\nu(0.6\mu\text{m}) = 94$ compared to 9.7 for Mrk 231). However, the mid-IR ($10\mu\text{m}$) over radio flux ratios are very similar and the mid-IR ($10\mu\text{m}$) over X-ray flux is only 3 times higher in SW104409 than in Mrk 231.

The X-ray and near-IR properties of SW104409 indicate that the source is heavily obscured. However, the observed optical continuum is blue and the spectrum shows emission lines with broad

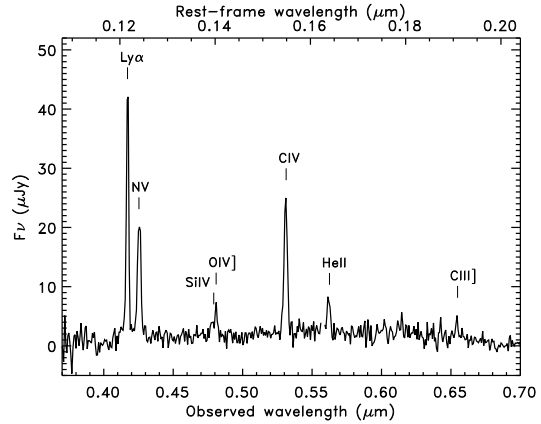


Fig. 7.— Optical spectrum of SW104406 obtained with the Keck I telescope. Detected emission features are labeled

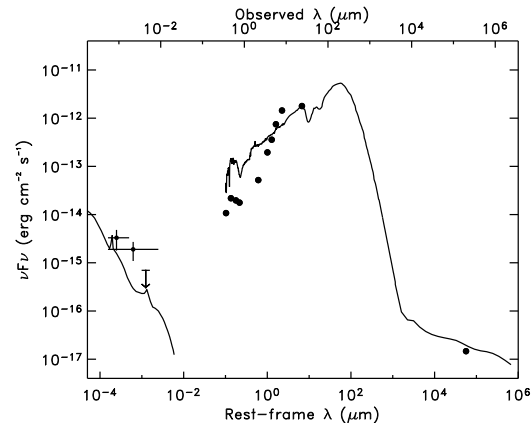


Fig. 8.— SED of SW104409 (black circles) compared to the SEDs of the Compton-thick AGN (black curve), Mrk 231, normalized at the observed $24\mu\text{m}$ flux. The crosses correspond to the observed X-ray flux in the broad, and hard X-ray bands. The downward arrow is the 2σ upper limit to the soft-X-ray flux. The X-ray flux energy range is indicated by the length of the horizontal line. The X-ray fluxes are derived assuming an absorbed power-law model with photon index, Γ equal to 1.7 and Galactic absorption, $N_{\text{H}} = 6 \times 10^{19} \text{ cm}^{-2}$.

components. A plausible explanation for the observed optical spectrum could be scattering. The scattered light preserves the spectral shape of the intrinsic component, but its flux corresponds to a fraction of the primary component which depends on the covering factor of the scattering medium (Smith et al. 2003). The fraction of scattered radiation can be estimated by comparing the

observed and the intrinsic (unabsorbed) optical flux. Since the observed optical spectrum is similar to that observed in optically selected quasars and scattering does not modify the spectral shape of the intrinsic spectrum, we estimated the intrinsic optical flux by assuming that the intrinsic, before absorption, SED of SW104409 is similar to that of an unobscured QSO normalized at the observed mid-IR observed flux. In Figure 9, we show the SED of SW104409 and an unobscured QSO template in three cases: 1) normalized at the observed $24\mu\text{m}$ flux of SW104409 to represent the intrinsic, before absorption, emission of SW104409; 2) scaled to match the observed optical data, to represent the scattered component, and 3) reddened by an extinction $A_V=4$ mag ($E(B-V)\simeq 1$). Reddening was applied as prescribed in Calzetti & Heckman (1999) assuming a foreground screen of dust at the redshift of the source. According to this scenario, SW104409 resembles an optically selected quasar whose light is reddened by an extinction $A_V=4$ mag and, therefore, completely suppressed at the observed optical wavelengths (ultraviolet in the rest-frame) and reddened in the near-IR (optical in the rest-frame). Assuming that the observed optical blue spectrum is due to scattering, the scattered fraction corresponds to 0.6% of the intrinsic optical emission.

Note that throughout this work, we apply reddening as prescribed in Calzetti & Heckman (1999). We also investigated the use of the Small Magellanic Cloud (SMC) extinction curve (Prevot et al. 1984; Bouchet et al. 1985) that well reproduces the optical spectra of dust reddened quasars in SDSS (Richards et al. 2003). The two prescriptions produce similar reddening at $\lambda > 5000\text{\AA}$, but the SMC law produces redder spectra at shorter wavelengths for the same amount of extinction.

Different geometries of the obscuring material were investigated by comparing the observed SED of SW104409 with predictions from radiative transfer models within the AGN unification scenarios. The models assume that the absorbing material is distributed in a toroidal shape around the central heating source. Two geometries were taken into account, flared and tapered disks, as described in detail in Efstathiou & Rowan-Robinson (1995). In flared disks the thickness of the disk increases linearly with distance from the central source. In tapered disks the thickness of

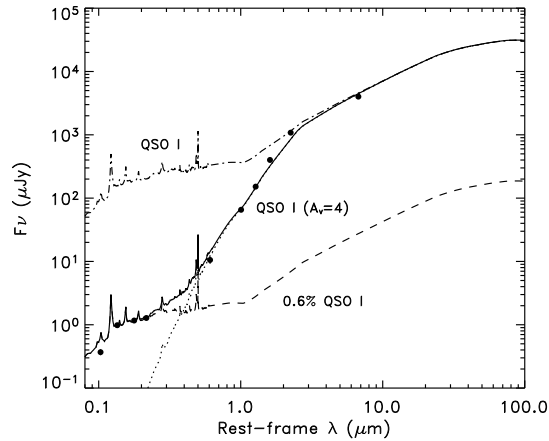


Fig. 9.— Observed SED of SW104409 (black circles) compared to an unobscured QSO template: 1) normalized to the mid-IR flux of SW104409 (dashed-dotted curve), 2) scaled to match the optical flux of SW104409 (dashed line), and 3) extinguished by $A_V=4$ to fit the IR data points (solid curve) (see section 4.1). The solid curve corresponds to the sum of the extinguished (3) and the scattered components (2).

the disk in the inner part also increases linearly with distance from the source but stays constant in the outer part. We find that a good fit to the rest-frame ultraviolet to mid-IR spectrum of SW104409 can be obtained with a tapered disk with an opening angle of 60 degrees. The predicted SED for this model is shown in Figure 10 and compared to the observed SED of SW104409. The predicted inclination of the line of sight with respect to the disk axis (61 degrees) implies that it is almost grazing the boundaries of the torus. The line of sight optical depth at 1000\AA rest-frame through the torus is 700 which corresponds to an optical depth $\tau_V=129$ or $A_V=140$. The best-fit model also assumes that the emission from the torus suffers additional extinction of 0.5 magnitudes by dust which is located at some distance from the nucleus; e.g. in the host galaxy. The predicted optical emission, which well agrees with the observed optical data, is produced by light scattered by the torus.

Due to the high optical depth to the central source, the optical emission must be scattered light. According to this model, scattering takes place in the inner walls of the disk and its surface, therefore, in order to observe scattered light the inclination must be slightly larger than the open-

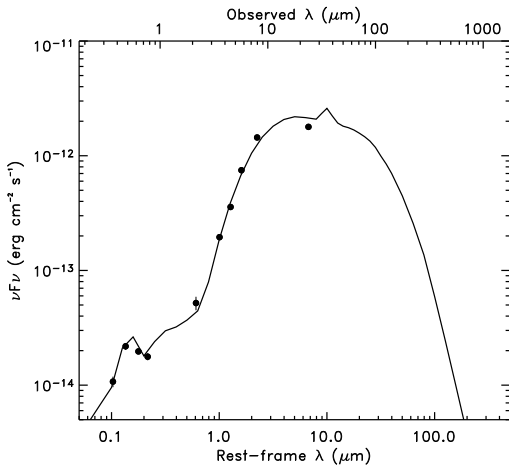


Fig. 10.— Observed SED of SW104409 (black circles) compared to a model of tapered disk with opening angle of 60° , optical depth $\tau_V=129$ and line of sight inclination of 61° (black solid curve).

ing angle of the disk. In case of larger inclination angles, the disk would obscure the scattered light. For inclination angles smaller than the opening angle, the scattered light would still be visible, however this geometry would be inconsistent with the obscured nature of this source. The similarity between the inclination and opening angles is also suggested by the observed $1-10\mu\text{m}$ SED, characteristic of emission from hot dust. Since the scattering region and the hot dust region are almost co-spatial, the inclination must be similar to the opening angle, otherwise the disk would obscure the emission from this region. An alternative to this model is scattering produced by electrons or dust in the opening cone of the accretion disk, instead than from the walls of the disk. In this case the similarity between the opening and inclination angles is not required, however it would still be required to explain the shape of the near- to mid-IR continuum. This model is consistent with the simple scenario described above. The large difference in the amount of extinction is likely due to the different assumptions made for the dust distribution. In the simple model of scattering+obscured QSO, we assume a foreground screen of dust absorbing the emitted radiation. This assumption does not take into account re-emission from dust and produces an underestimation of the dust opacity. Radiative transfer models are more accurate

in estimating the dust opacity since they take into account the transmission of the intrinsic radiation through the dusty material. According to the results from the radiative transfer model and assuming a Galactic dust to gas ratio, the estimated gas column density surrounding the central regions is $\sim 2.6 \times 10^{23} \text{ cm}^{-2}$, consistent with what is observed in the X-ray. However, since the X-ray emission is produced in the nucleus and the optical and near-IR radiation are emitted in the outer regions, the absorbing gas intercepted by the X-ray photons is expected to be closer to the disk plane and have a larger column density than the material intercepted by the optical/near-IR radiation. In spite of its simplicity, the proposed picture reconciles the multiwavelength observations of SW104409 and agrees well with the unification model.

5.2. SW104406

The spectral energy distribution (SED) of SW104406 is shown in Figure 11. The optical spectrum is characterized by a blue continuum as in the case of SW104409 with no indication for intrinsic reddening. As in the case of SW104409, the optical data are characterized by a U-band drop-out which is probably caused by IGM attenuation. SW104406 also fits within the conventional definition of EROs with an observed $r'-K_s=4.82$ (Vega). Its SED is very similar to the SED of Mrk 231 after applying an additional extinction of $A_V=0.2$ as shown in Figure 12. The optical spectrum can be fitted with this reddened template and an additional component, as scattered light, is not required by the data. The X-ray over IR ratio of SW104406 is about 10 times higher than for Mrk 231, but the X-ray spectrum is similarly hard or even harder. Contamination from stellar light emission from the host galaxy or a starburst, which would appear as a broad bump with a peak at $\lambda^{rest} \sim 1.6\mu\text{m}$ in not observed.

In summary, both sources show SEDs where the AGN dominates at all observed wavelengths and any contribution from other energy source is negligible. The observed SED are both consistent with a scenario in which the optical and near-IR sources are obscured. In the X-rays, the observed spectrum is likely due to the transmitted direct component seen through Compton-thick matter.

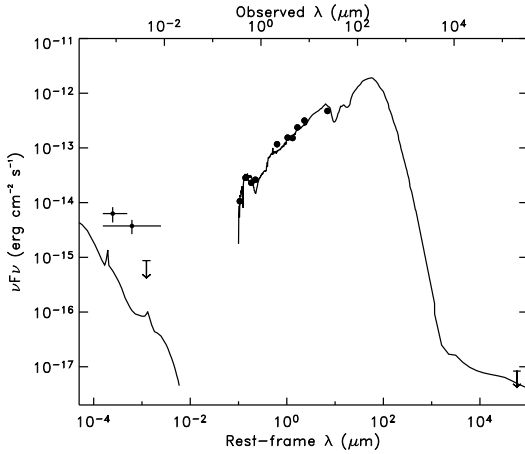


Fig. 11.— SED of SW104406 (black circles) compared to the SED of the Compton-thick Seyfert 1 Mrk 231 normalized at $24\mu\text{m}$ with an $A_V=0.2$ mag additional extinction (black curve). The crosses correspond to the observed X-ray flux in the broad, and hard X-ray bands. The downward arrow is the 2σ upper limit to the soft-X-ray flux. The X-ray flux energy range is indicated by the length of the horizontal line. The X-ray fluxes are derived assuming an absorbed power-law model with photon index, Γ equal to 1.7 and Galactic absorption, $N_{\text{H}}=6\times10^{19}\text{ cm}^{-2}$.

6. Luminosity, Black-Hole Mass and Accretion Rate of SW104409 and SW104406

The luminosities as a function of wavelength of SW104406 and SW104409 are shown in Figures 12 and 13, respectively. The luminosity distribution of the unobscured quasar template, “Elvis QSO” (Elvis et al. 1994) normalized to the mid-IR flux of the two quasars is also shown for comparison. The template is also shown after applying enough extinction to reproduce the red IR SEDs of SW104409 and SW104406.

Due to the lack of data at $\lambda_{\text{rest}} > 7\mu\text{m}$ we cannot directly measure the total IR luminosity, but we can derive it making some assumptions about the SED shape. Assuming the model shown in Figure 9 for SW104409 and a reddened ($AV=0.2$) Mrk 231 for SW104406 at $\lambda = 7 - 1000\mu\text{m}$, the IR luminosities, $L(3-1000\mu\text{m})$, are $3.4\times10^{47}\text{ ergs s}^{-1}$ ($=8.8\times10^{13}\text{ L}_\odot$) and $1.2\times10^{46}\text{ ergs s}^{-1}$ ($=3.1\times10^{12}\text{ L}_\odot$), respectively. SW104409 is a hyper-luminous IR galaxy (HYLIRG) and SW104406 an ultra-luminous IR galaxy (ULIRG) (Sanders & Mirabel 1996). The integrated luminosities in different wavelength ranges, as well as the bolometric luminosity of

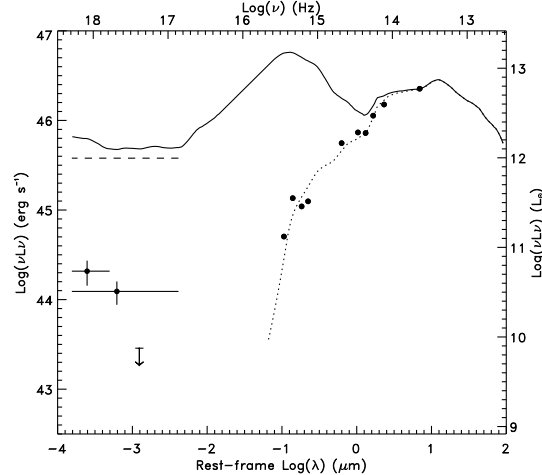


Fig. 12.— SED in νL_ν of SW104406 (black full circles) compared to Elvis QSO template normalized at $24\mu\text{m}$ in two cases: 1) with no additional extinction (black solid curve) and 2) with 1.7 mag additional extinction (black dotted curve). The dashed line corresponds to the absorption-corrected broad band X-ray luminosity. The crosses correspond to the X-ray luminosities in the broad, and hard X-ray bands. The downward arrow is the 2σ upper limit to the soft-X-ray luminosity. The X-ray energy range is indicated by the length of the horizontal lines.

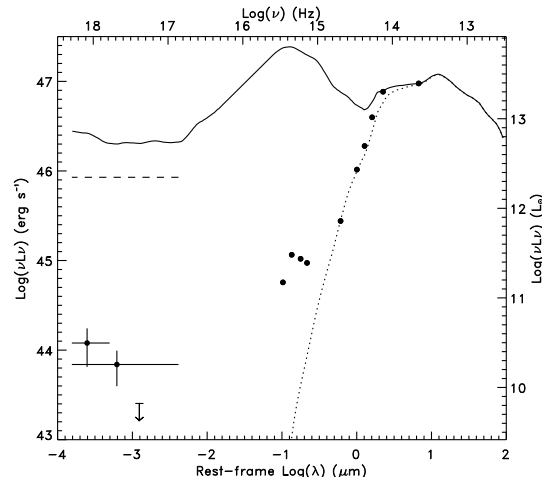


Fig. 13.— SED in νL_ν of SW104409 (black full circles) compared to Elvis QSO template normalized at $24\mu\text{m}$ in two cases: 1) with no additional extinction (black solid curve) and 2) with 4.0 mag additional extinction (black dotted curve). The dashed line corresponds to the absorption-corrected broad band X-ray luminosity.

both sources are listed in Table 11. The radio luminosity is derived assuming the radio spectral

index typically observed in AGN, $\alpha = -0.8$ (Condon 1988), where $F_\nu \propto \nu^\alpha$. The implied rest-frame 1.4 GHz radio luminosity density of SW104409 is $L_{1.4\text{GHz}} = 5.3 \times 10^{31} \text{ ergs s}^{-1} \text{ Hz}^{-1}$, and less than $3.0 \times 10^{31} \text{ ergs s}^{-1} \text{ Hz}^{-1}$ for SW104406. These high radio powers are a signature of the presence of an AGN.

The bolometric luminosity can be derived by adding the absorption-corrected X-ray luminosity, the estimated radio luminosity (only in the case of SW104409) and the optical-IR luminosity. The derived bolometric luminosities are $3.9 \times 10^{47} \text{ ergs s}^{-1}$ ($1.0 \times 10^{14} L_\odot$) for SW104409 and $1.9 \times 10^{46} \text{ ergs s}^{-1}$ ($4.6 \times 10^{12} L_\odot$) for SW104406. Because of the uncertainty associated with the lack of data above $\lambda^{rest} = 7\mu\text{m}$, we derived a lower limit to the bolometric luminosity by replacing the optical-IR luminosity $L(0.03 - 1000\mu\text{m})$ with $L(0.03 - 10\mu\text{m})$. The obtained values are a factor of 2 lower than the estimates obtained by extrapolating the model to $\lambda > 10\mu\text{m}$ (see values in Table 11). The absorption-corrected X-ray luminosities of SW104409 and SW104406 correspond, respectively, to $\sim 1\%$ and 30% of their bolometric luminosity.

Assuming that the AGN is the main source of the observed bolometric luminosity and that it is accreting at the Eddington limit ($L_{bol} = L_{Edd}$), the estimated black-hole mass for SW104409 and SW104406 is $\simeq 2.9 \times 10^9 M_\odot$ and $1.4 \times 10^8 M_\odot$, respectively, or $1.2 \times 10^9 M_\odot$ and $6.6 \times 10^7 M_\odot$, if we do not include the energy emitted at $\lambda > 10\mu\text{m}$ in the estimate of the AGN bolometric luminosity. If we assume an accretion efficiency of 10%, the derived accretion rates are $68 M_\odot \text{ yr}^{-1}$ for SW104409 and $3.4 M_\odot \text{ yr}^{-1}$ for SW104406, or $28 M_\odot \text{ yr}^{-1}$ for SW104409 and $1.5 M_\odot \text{ yr}^{-1}$ for SW104406 if we do not include the energy emitted at $\lambda > 10\mu\text{m}$ in the estimate of the AGN bolometric luminosity. The black-hole mass of SW104409 is comparable to the highest measured values in the local Universe, i.e. M87 (Ford et al. 1994) and Cyg A (Tadhunter et al. 2003) having $M_{BH} \simeq 3 \times 10^9 M_\odot$. Its accretion rate is also among the highest observed in quasars at $z \leq 2$ (McLure & Dunlop 2004). SW104406 is also characterized by a large black-hole mass and accretion rate, but it is not as extreme as SW104409. Since most of the quasars accrete below their Edding-

ton limit (McLure & Dunlop 2004), it would be more realistic to assume a lower Eddington ratio, however, this would imply even higher black hole masses.

7. Comparison with other Compton-thick AGN at $z \gtrsim 2$

Only a few Compton-thick quasars at $z \gtrsim 2$ are currently known. Here, we compare their properties with those of SW104409 and SW104406 and investigate whether they represent the same population or if the different selection methods are finding objects with different properties. The largest and probably best sampled sample of Compton-thick AGN currently known contains 4 sources (Alexander et al. 2005a,b). These sources were drawn from an X-ray detected sub-millimeter selected sample in a 0.12 deg^2 field. Optical data from HST, IR data from *Spitzer*, radio data and optical high-resolution spectra are available for all of the sources. Spectroscopic redshifts range from 2 to 2.5 and broad-band (0.5-8 keV) X-ray fluxes range from 0.7 to $1.3 \times 10^{-15} \text{ ergs cm}^{-2} \text{ s}^{-1}$. These sources host both an AGN and a powerful starburst, and their optical-near-IR SEDs are dominated by stellar light (Borys et al. 2005). The optical spectra of all sources are also dominated by a starburst component (Chapman et al. 2005). The AGN bolometric luminosities, estimated from the observed X-ray flux after correcting it for absorption, range from 2.2 to $4.4 \times 10^{11} L_\odot$, the derived black-hole masses range from 0.6 to $1.6 \times 10^7 M_\odot$ and the accretion rates vary from 0.13 to $0.35 M_\odot/\text{yr}$. The main differences between this sample and the two obscured quasars SW1044090 and SW104406 is in the AGN bolometric luminosity, and thus in the accretion rates and the black-hole masses which are, on average, two order of magnitudes lower. Another important difference is in the presence of a dominant starburst component which is absent or negligible in SW104409 and SW104406. It is clear that the two quasars presented in this work and these AGN/sub-millimeter galaxies show some major differences and might be very different objects. However, before deriving any conclusions on the differences between these two samples, we should evaluate how the different methods applied to estimate the AGN bolometric luminosity affect these results.

We tried to reproduce Alexander et al. (2005b)'s estimates using their energy ranges and found that their correction for absorption to the rest-frame X-ray luminosity is about 4 times smaller than ours for $N_{\text{H}}=10^{24} \text{ cm}^{-2}$. The most likely explanation for the observed difference is the difference in the assumed X-ray model used to derive the K-correction. Alexander et al. (2005a,b) adopt a model which includes an absorbed power-law component with $\Gamma=1.8$, a neutral reflection component, a scattered component of ionized gas, and a Fe K α emission line at 6.4 keV. We also notice a discrepancy in the column density estimates, their values being on average 2.5 times larger than what we would predict with our method. Although this would yield larger luminosities, their correction factor due to the different spectral model is much smaller than ours, thus their absorption-corrected rest-frame luminosities are lower than what we would estimate. If we apply our method to their sample, the derived absorption-corrected rest-frame X-ray luminosities are, on average, higher by a factor of 8 (from 3 to 12.5 times higher). Their smaller X-ray luminosities imply smaller AGN bolometric luminosities, black-hole masses and accretion rates by the same factors. A third difference between our methods is in the derivation of bolometric luminosity. They assume a constant factor between the absorption-corrected rest-frame X-ray luminosity and the bolometric luminosity of 6%, while we add the luminosity measured throughout the whole spectrum (30% for SW104409 and 1% for SW104406; see Section 6). Even after correcting by the factors described above, the differences in AGN luminosity, SMBH mass and accretion rate between the two quasars presented in this work and the sample in Alexander et al. (2005a,b) are still significant, more than one order of magnitude compared to almost two order of magnitude initially measured. Thus, we conclude that the four sources in Alexander et al. (2005b) and our two quasars are different.

Other examples of Compton-thick AGN at high- z are the type 2 quasars, CXO-52 ($z=3.288$; Stern et al. (2002)), CDFS-202 ($z=3.700$; Norman et al. (2001)) and CDFS-263 ($z=3.660$; Mainieri et al. (2005)). The former two sources show similar characteristics to SW104409 and SW104406. The X-ray selected type 2 QSO detected at sub-

millimeter wavelengths, CDFS-263, is instead more similar to the sub-millimeter selected AGN discussed above. The SEDs of these quasars at $\lambda > 2.5 \mu\text{m}$ are not currently available, but at shorter wavelengths CXO-52 and CDFS-202 show very similar SEDs to those of SW104409 and SW104406 with AGN-dominated optical spectra and red optical-near-IR colors. Assuming that the absorption-corrected X-ray luminosity corresponds to 10% of the AGN bolometric luminosity (Elvis et al. 1994), we derive a bolometric luminosity, L_{bol} , of $3.3 \times 10^{45} \text{ ergs s}^{-1}$ for CXO-52 and of $2 \times 10^{46} \text{ ergs s}^{-1}$ for CDFS-202. Assuming accretion at the Eddington limit, the black-hole masses are $2.5 \times 10^7 \text{ M}_{\odot}$ and $1.1 \times 10^8 \text{ M}_{\odot}$ respectively. These values are also lower than what we derive for SW104409 and similar to those derived for SW104406, but higher than those measured in (Alexander et al. 2005a)'s sub-millimeter selected Compton-thick AGN. In CXO-52 and CDFS-202, as in SW104409 and SW104406, the AGN dominates over the host galaxy and the associated luminosity and SMBH mass are one order of magnitude higher than observed in sub-millimeter selected Compton-thick AGN.

The two Compton-thick AGN discussed in this work also differ from a sample of high- z , heavily obscured, and luminous AGN candidates selected at IR and radio wavelength (Martínez-Sansigre et al. 2005). We applied the same selection criteria to the complete IR and X-ray samples, to the IR-selected obscured AGN candidates and to the X-ray selected Compton-thick AGN in Figure 14. Only one source among the IR-selected obscured AGN candidates satisfies their selection criteria, SWIRE_J104641.38+585213.9 and none of the X-ray selected Compton-thick AGN. Although the two Compton-thick AGN, SW104409 and SW104406, are luminous and obscured AGN at $z > 2$ (see section 4), they do not pass either the $3.6 \mu\text{m}$ or the radio limit (see large black circles in Figure 14) required by Martínez-Sansigre et al. (2005). In the entire field only 6 sources satisfy their selection criteria, of which 2 show power-law like IR SEDs and are also detected in the X-ray. One is SWIRE_J104641.38+585213.9 which we classify as class III source (see table 4), the other source is characterized by an SED consistent with an unobscured QSO. The remaining 4 sources are characterized by SEDs more similar to

those in class IV. Although both selection methods are based on IR-colors derived from *Spitzer* there is little overlap among the two samples.

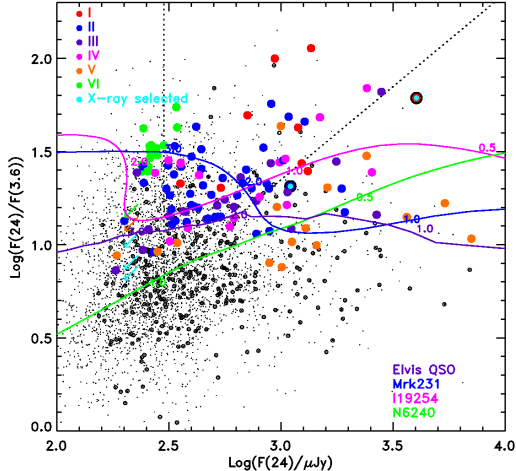


Fig. 14.— IR color $F(24\mu\text{m})/F(3.6\mu\text{m})$ versus the IR flux at $24\mu\text{m}$ for the IR (black dots) and X-ray (black open circles) sources detected at 3.6 and $24\mu\text{m}$ in the *Chandra*/SWIRE field. IR-selected obscured AGN candidates are shown as full circles with colors corresponding to different SED types (I:red, II:blue, III:purple, IV:magenta, V:orange, and VI:green). Symbols as in Figure 4. X-ray selected obscured AGN are shown as cyan full circles and as cyan arrows if non-detected at $24\mu\text{m}$. The dotted line defines the IR selection criteria used in Martinez-Sansigre et al. (2005) for obscured AGN at high- z .

A compilation of all heavily obscured AGN selected by different methods and a systematic analysis of their multi-wavelength properties is necessary to understand the differences among these sources and their origin, e.g. a different evolutionary stage, SMBH mass, accretion rate or environment.

8. Statistical predictions for Compton-thick AGN

The two selection methods described in Sections 3.1 and 3.2 were defined for samples of obscured AGN based on their X-ray and optical-IR properties, respectively. The X-ray selected sample includes X-ray detected AGN with hard X-ray spectra and estimated column densities $\geq 10^{24}\text{ cm}^{-2}$ (5 sources). The IR-selected sample contains AGN with red optical-IR colors and whose emission dominates in the near- and mid-IR over

the host galaxy light (120 sources). The first selection method is biased against Compton-thick AGN whose primary X-ray radiation is completely absorbed in the observed energy range, i.e. sources at low- z or with column densities $\geq 10^{25}\text{ cm}^{-2}$, and against sources that are fainter than $10^{-15}\text{ ergs cm}^{-2}\text{s}^{-1}$ at $0.3\text{-}8\text{ keV}$. The second method is biased against AGN that are too faint to be detected in 3 IR bands at our sensitivity limits or whose host galaxy is brighter than the AGN in the optical-IR wavelength range. Because of these selection effects, we can only estimate a lower limit to the surface density of IR detected Compton-thick AGN in the *Chandra*/SWIRE field.

In the sub-sample of 41 IR-selected obscured AGN candidates which are detected in the X-rays, only two sources, $\sim 5\%$, are confirmed Compton-thick AGN, SW104409 and SW104406. If we assume that this fraction does not depend on the X-ray flux and is the same for the entire IR selected sample of obscured AGN candidates (but see discussion in Section 3.2.3), we estimate about 6 sources (5% of 120 sources) to be Compton-thick AGN. Since only two out of five X-ray selected Compton-thick AGN are also selected by the IR-selected criteria, we assume that our IR selection identifies only 40% (2 out of 5) of all Compton-thick AGN in the field. Thus, the estimated total number of Compton-thick AGN in the field is about 15 ($\simeq 6/0.4$) or 25 sources deg^{-2} . The estimated number of sources (15) should be considered a lower limit to the total number of Compton-thick AGN detected in the IR at our sensitivity limits in the *Chandra*/SWIRE field. Due to the lack of X-ray data for most of the sources, the identification of these 15 Compton-thick AGN is not possible because of lack of constraints on their column densities. The only exceptions are the 5 X-ray selected Compton-thick AGN presented in Section 3.1. The fraction of Compton-thick AGN detected in the X-ray at our depth ($F(0.3\text{-}8\text{ keV}) \geq 10^{-15}\text{ ergs cm}^{-2}\text{s}^{-1}$) is 33% (5 out of 15). This fraction is consistent with the value estimated by Treister et al. (2004) of 30% of all Compton-thick AGN detected at the X-ray limit of the *Chandra* deep surveys.

We compared our results with the number of obscured AGN detected in the IR and in the X-rays predicted by various models (Silva, Maiolino & Granato 2004; Treister & Urry 2005; Xu et

al. 2003; Polletta et al. 2003). Since our selection is very similar to a $24\mu\text{m}$ flux selection, we compared our results with those predicted for AGN with a $24\mu\text{m}$ flux greater than our 5σ limit, $230\mu\text{Jy}$. However, our selection is more restricted due to the additional requirements on the properties of the IR SED and, therefore, we expect our numbers to be lower than those expected from a limited-flux sample of AGN. Silva, Maiolino & Granato (2004) predicts about 670 AGN deg^{-2} , of which 500 are obscured ($\text{N}_\text{H} \geq 10^{22} \text{ cm}^{-2}$) (obscured:unobscured=2.9:1) and about 300 are Compton-thick. Treister & Urry (2005) predicts about $1000 \text{ AGN deg}^{-2}$, of which 765 are obscured ($\text{N}_\text{H} \geq 10^{22} \text{ cm}^{-2}$) (obscured:unobscured=3:1) and no prediction for Compton-thick AGN is given. Xu et al. (2003) and Polletta et al. (2003) predict about $1100 \text{ AGN deg}^{-2}$, of which 810 are obscured ($\text{N}_\text{H} \geq 10^{22} \text{ cm}^{-2}$) (obscured:unobscured=2.8:1). Although these models are different and have not been fully tested with respect to the available IR and X-ray observables, they are all consistent with a surface density of about $700\text{--}1000 \text{ AGN deg}^{-2}$, a ratio between obscured and unobscured AGN of 3:1, and about 300 Compton-thick AGN. Our IR selection of AGN yields 120 ($\sim 200 \text{ deg}^{-2}$) obscured AGN candidates and 61 ($\sim 100 \text{ deg}^{-2}$) unobscured AGN candidates, corresponding to only about 20% of the expected number of AGN, and to an obscured to unobscured ratio of $\sim 2:1$. The total number of AGN and the ratio between obscured and unobscured AGN would likely increase if the selection was not limited to sources with AGN-dominated and red IR SEDs. Our lower limit to the surface density of Compton-thick AGN is less than 10% the expected value, indicating that even in the mid-IR a large fraction of these sources are elusive.

9. Conclusions

Theoretical models, simulations and indirect observations predict the presence of a large population of highly obscured luminous AGN at moderate and high redshifts. The quest for these objects has been hindered by the difficulty of detecting and identifying them and, thus, very few examples are currently known. In this work, we show how the combined high sensitivity and spatial resolution of the *Spitzer* Space Telescope and of the *Chandra* X-ray Observatory are overcoming these

difficulties, offering the capability of detecting and identifying heavily obscured AGN up to high redshifts, providing constraints on their surface density and characterizing their properties.

Using the dataset in the *Chandra*/SWIRE field (0.6 deg^2 in the Lockman Hole), we conducted a search for Compton-thick AGN. We selected, independently, two samples of Compton-thick AGN candidates based on their X-ray spectral properties and optical-IR SED. The X-ray and IR selected samples contain, respectively, 5 and 120 sources. Based on the properties of the X-ray selected Compton-thick AGN, we estimate that only 40% of the population of heavily obscured AGN shows distinct AGN signatures in their optical-IR SEDs, the rest being dominated by the host-galaxy emission. The number of Compton-thick AGN detectable in the *Chandra*/SWIRE field is of at least 25 sources deg^{-2} and only 33% of them are detected in the X-ray down to a flux limit of $10^{-15} \text{ ergs cm}^{-2} \text{ s}^{-1}$. The X-ray over optical flux ratios of the selected obscured AGN cover a similar range as the rest of the X-ray sample and well overlap with those observed for “classical” AGN, indicating that searches for heavily obscured AGN among X-ray sources with extreme X-ray over optical flux ratios might miss a large fraction of these sources.

The complete sample of AGN selected on the basis of a red power-law like IR SED contains 181 sources, of which 61 show SEDs similar to those of unobscured AGN, and 120 are obscured AGN candidates. The complete sample corresponds to only about 20% of the total number of AGN expected to be detected in the mid-IR at our sensitivity. The observed ratio between obscured and unobscured AGN is 2:1, still lower than the models predictions, $\sim 3:1$. The estimated surface density of Compton-thick AGN is only 10% the expected value. These results suggest that even in the mid-IR, heavily obscured AGN are elusive.

Optical spectroscopy of two obscured AGN candidates confirmed that they are high redshift, SW104409 at $z=2.54$ and SW104406 at $z=2.43$, Compton-thick QSOs. These sources, characterized by type 2 AGN spectra, very red optical-IR SEDs and high X-ray luminosities ($\sim 10^{45} \text{ ergs s}^{-1}$), have properties (SEDs, luminosities and SMBH masses) similar to those observed in the high- z Compton-thick quasars CXO-52

($z=3.288$; Stern et al. (2002)), and CDFS-202 ($z=3.700$; Norman et al. (2001)). However, they differ from sub-millimeter selected Compton-thick AGN (Alexander et al. 2005b) where emission from a starburst dominates at most wavelengths and black-hole masses and accretion rates are one order of magnitude lower. SW104409 represents the most luminous ($\sim 10^{14} L_\odot$) Compton-thick QSOs at high- z currently known with a SMBH mass comparable to the most massive local SMBH ($\sim 3 \times 10^9 M_\odot$). Such a rare object can be found when large volumes are sampled as in the SWIRE/*Chandra* field ($\sim 0.6 \text{ deg}^2$).

M.P. thanks Alain Omont and Dan Weedman for useful discussions. This work is based on observations made with the *Spitzer Space Telescope*, which is operated by the Jet Propulsion Laboratory, California Institute of Technology under NASA contract 1407. Support for this work, part of the *Spitzer Space Telescope* Legacy Science Program, was provided by NASA through an award issued by the Jet Propulsion Laboratory, California Institute of Technology under NASA contract 1407. MP, BW and RK are grateful for the financial support of NASA grant G04-5158A (*Chandra*). BW is grateful for the financial support of NASA contract NAS8-39073 (*Chandra*X-ray Center).

This research makes use of the NASA/IPAC Extragalactic Database (NED) which is operated by the Jet Propulsion Laboratory, California Institute of Technology, under contract with the National Aeronautics and Space Administration. Based on observations obtained at the Hale Telescope, Palomar Observatory as part of a continuing collaboration between the California Institute of Technology, NASA/JPL, and Cornell University. This publication makes use of data products from the Two Micron All Sky Survey, which is a joint project of the University of Massachusetts and the Infrared Processing and Analysis Center/California Institute of Technology, funded by the National Aeronautics and Space Administration and the National Science Foundation.

Facilities: Spitzer(IRAC,MIPS), CXO(ACIS).

REFERENCES

Akiyama, M., Ueda, Y., Ohta, K., Takahashi, T., & Yamada, T. 2003, ApJS, 148, 275

Alexander, D. M., La Franca, F., Fiore, F., Barcons, X. et al., 2001, ApJ, 554, 18

Alexander, D. M., Bauer, F. E., Chapman, S. C., Smail I., Blain, A. W., & Ivison, R. J. 2005a, ApJ, 632, 736

Alexander, D. M., Smail, I., Bauer, F. E., Chapman, S. C. et al. 2005b, *Nature*, 434, 738

Alonso-Herrero, A., Pérez-González, P. G., Rigby, J., Rieke, G. H et al. 2004, ApJS, 154, 155

Alonso-Herrero, A., Pérez-González, P. G., Alexander, D. M., Rieke, G. H et al. 2005, ApJ accepted, (astro-ph/0511507)

Antonucci, R., 1993, ARA&A, 31, 473

Babbedge, T.S.R. 2004a, PhD Thesis, Imperial College, London, U.K.

Babbedge, T.S.R. et al. 2004b, MNRAS, 353, 654

Barger, A. et al. 2002, ApJ, 124, 1839

Barger, A. J., Cowie, L. L., Mushotzky, R. F., Yang, Y., Wang, W.-H., Steffen, A. T. & Capak, P. 2005, AJ, 129, 578

Bassani, L., Dadina, M., Maiolino, R., Salvati, M., Risaliti, G., Della Ceca, R., Matt, G. & Zamorani, G. 1999, ApJS, 121, 473

Berta, S., Fritz, J., Franceschini, A., Bressan, A., & Pernechele, C. 2003, A&A, 403, 199

Bertin, E., & Arnouts, S. 1996, A&AS, 117, 393

Bolzonella M., Miralles J.-M. & Pelló R. 2000, A&A, 363, 476

Borys, C., Smail, I., Chapman, S. C., Blain, A. W., Alexander, D. M., & Ivison, R.J. 2005, ApJ accepted (astro-ph/0507610)

Bouchet, P., Lequeux, J., Maurice, E., Prevot, L., & Prevot-Burnichon, M. L. 1985, A&A, 149, 330

Braito, V., Franceschini, A., Della Ceca, R., Severgnini, P. et al. 2003, A&A, 398, 107

Braito, V., Della Ceca, R., Piconcelli, E., Severgnini, P. et al. 2004, A&A, 420, 79

Calzetti, D. & Heckman, T. M. 1999, ApJ, 519, 27

Cattaneo, A., Blaizot, J., Devriendt, J. & Guiderdoni, B. 2005, MNRAS, 364, 407

Chapman, S. C., Blain, A. W., Smail, I., & Ivison, R. J. 2005, ApJ, 622, 772

Comastri, A., Setti, G., et al., 1995, A&A, 296, 1

Comastri, A., Brusa, M., & Mignoli, M. 2003, Astron. Nachr., 324, 28

Comastri, A., 2004 in “Supermassive Black Holes in the Distant Universe”, ed. A. J. Barger, Kluwer Academic Press (astro-ph/0403693)

Condon, J.J. 1988, in “Galactic and Extragalactic Radio Astronomy”, Second edition, eds. G. L. Verschuur and K. I. Kellermann (Springer-Verlag), 641

Cutri, R. M., Nelson, B. O., Francis, P. J., & Smith, P. S. 2002, Proceedings of IAU Colloquium 184, ASP Conference Proceedings, 284, 127

Cutri, R. M., et al. 2003, Explanatory Supplement to the 2MASS All Sky Data Release (Pasadena: Caltech)

Della Ceca, R., Maccacaro, T., et al., 2004, A&A, 428, 383

De Luca, A., Molendi, S., 2004, A&A, 419, 837

Dickey, J. M. & Lockman, F.J. 1990, ARA&A, 28, 215

Di Matteo, T., Springel, V., & Hernquist, L. 2005, *Nature*, 433, 604

Donley, J. L., Rieke, G. H., Rigby, J. R., Pérez-González, P. G. 2005, ApJ, 634, 169

Dwelly, T., Page, M. J., Loaring, N. S., Mason, K. O. et al. 2005, MNRAS, 360, 1426

Efstathiou, A., & Rowan-Robinson, M. 1995, MNRAS, 273, 649

Elston, R., Rieke, G. H. and Rieke, M. J. 1988, ApJ, 331, 77

Elvis, M., Wilkes, B. J., McDowell, J. C. et al. 1994, ApJS, 95, 1

Fabian, A. C. 1999, MNRAS, 308, L39

Fadda, D., Flores, H., Hasinger, G., Franceschini, A. et al. 2002, A&A, 383, 838

Fazio, G. G., et al. 2004, ApJS, 154, 10

Fiore, F. et al. 2003, A&A, 409, 79

Ford, H.C. et al. 2004, 1994, ApJ, 435, L27

Franceschini, A., Manners, J., Polletta, M. et al. 2005, AJ, 129, 2074

Freeman, P. E., Doe, S., Siemiginowska, A. 2001, *SPIE Proceedings*, 4477, 76

Freeman, P. E., Kashyap, V., Rosner R., & Lamb, D. Q. 2002, ApJS, 138, 185

Gallagher, S. C., Richards, G. T., Hall, P. B., Brandt, W. N., Schneider, D. P., Vanden Berk, D. E. 2005, AJ, 129, 567

Granato, G., De Zotti, G., Silva, L., Bressan, A., Danese, L. et al. 2004, ApJ, 600, 580

Hao, L. et al. 2005, ApJ, 625, 75

Hatziminaoglou, E., Perez-Fournon, I., Polletta M. et al. 2005, AJ, 129, 1198

Houck, J. R., et al. 2005, ApJ, 622, 105

Hopkins, P. F., Hernquist, L., Martini, P., Cox, T. J., Robertson, B., Di Matteo, T., & Springel, V. 2005, ApJ, 625, 71

Iwasawa, K., Matt, G., Guainazzi, M., & Fabian, A.C. 2001, MNRAS, 326, 894

Kim, D-W., et al., 2004, ApJS, 150, 19

Kriss, G. A. 1994, ASP Conference Series, 61, 437, eds.: D.R. Crabtree, R.J. Hanisch, J. Barnes

Krolik, J. H. 1999, Active Galactic Nuclei: From the Central Black Hole to the Galactic Environment, Princeton University Press

La Franca, F. et al. 2005, ApJ, 635

Lacy, M. et al. 2004, ApJS, 154, 166

Longair, M. S. 1992, High Energy Astrophysics (Cambridge Univ. Press), Vol. 2

Lonsdale, C. J. et al. 2003, PASP, 115, 897

Lonsdale, C. J., Polletta, M., Surace, J., D., Fang, F., et al. 2004, ApJS, 154, 54

Lutz, D., Maiolino, R., Spoon, H. W. W., & Moorwood, A. F. M. 2004, A&A, 418, 465

Madau, P., Ghisellini, G., & Fabian, A. C. 1994, MNRAS, 270, L17

Madau, P. 1995, ApJ, 441, 18

Mainieri, V., Bergeron, J., et al., 2002, A&A, 393, 425

Mainieri, V. et al. 2005, MNRAS, 356, 1571

Maiolino, R., Rieke, G. H., 1995, ApJ, 454, 95

Maiolino, R., Comastri, A., Gilli, R., Nagar, N. M. et al. 2003, MNRAS, 344, L59

Manners, J. C., Serjeant, S., Bottinelli, S., Vaccari, M. et al. 2004, MNRAS, 355, 97

Martínez-Sansigre, A. et al. 2005, *Nature*, in press (astro-ph/0505486)

Massey, P., Strobel, K., Barnes, J.V., & Anderson, E. 1988, ApJ, 328, 315

Matt, G., Fabian, A. C., Guainazzi, M., Iwasawa, K., Basani, L., & Malaguti, G. 2000, MNRAS, 318, 173

McLure, R. J., & Dunlop, J. S. 2004, MNRAS, 352, 1390

Moran, E. C., Filippenko, A. V., & Chornock, R. 2002, ApJ, 579, L71

Moretti, A., Campana, S., et al., 2003, ApJ, 588, 696

Morrison, R., & McCammon, D. 1983, ApJ, 270, 119

Nandra, K., & Pounds, K. A. 1994, MNRAS, 268, 405

Norman, C. et al. 2002, ApJ, 571, 218

Oke, J. B., Cohen, J. G., Carr, M., Cromer, J. et al. 1995, PASP, 107, 375

Osterbrock, D. E., & Shaw, R. A. 1988, ApJ, 327, 89

Padovani, P., Allen, M. G., Rosati, P., & Walto, A. 2004, A&A, 424, 545

Peeters, E., Spoon, H. W. W., & Tielens, A. G. G. M. 2004, ApJ, 613, 986

Perola, G. C., Puccetti, S., et al., 2004, A&A, 421, 491

Piccinotti, G., Mushotzky, R. F., Boldt, E. A., Holt, S. S. et al. 1982, ApJ, 253, 485

Piconcelli, E., Cappi, M., et al., 2003, A&A, 412, 689

Polletta, M., Lonsdale, C. J., Xu, C. & Wilkes, B. J. 2003, AN, 324, 170

Prevot, M. L., Lequeux, J., Prevot, L., Maurice, E., & Rocca-Volmerange, B. 1984, A&A, 132, 389

Richards, G.T. et al. 2003, AJ, 126, 1131

Richards, G.T. et al. 2005, MNRAS, 360, 825

Rieke, G. et al. 2004, ApJS, 154,

Rigby, J. R. et al. 2004, ApJS, 154, 160

Rigby, J. R., Rieke, G. H., Pérez-González, P. G., Donley, J. L., Alonso-Herrero, A., Huang, J.-S., Barmby, P., & Fazio, G. G. 2005, *ApJ*, 627, 134

Rigopoulou, D., Spoon, H. W. W., Genzel, R. Lutz, D., Moorwood, A. F. M., & Tran, Q. D. 1999, *AJ*, 188, 2625

Risaliti, G., Maiolino, R., & Salvati, M. 1999, *ApJ*, 522, 157

Sanders, D. B., & Mirabel, I. F. 1996, *ARA&A*, 34, 749

Silk, J. & Rees, M. J. 1998, *A&A*, 331, L1

Silva, L., Maiolino, R., & Granato, G.L. 2004, *MNRAS*, 355, 973

Smith, D. A., & Done C. 1996, *MNRAS*, 280, 355

Smith, P. S., Schmidt, G. D., & Hines, D. C. 2003, *ApJ*, 593, 676

Spergel, D. N. et al. 2003, *ApJS*, 148, 175

Springel, V., Di Matteo, T., & Hernquist, L. 2005, *MNRAS*, 361, 776

Stern, D. et al. 2002, *ApJ*, 568, 71

Stern, D. et al. 2004, *ApJ*, 631, 163

Surace, J. A. et al. 2005, SWIRE Data Delivery Document II, *Spitzer* Science Center, Caltech

Szokoly, G. P. et al. 2004, *ApJS*, 155, 271

Tadhunter, C., Marconi, A., Axon, D., Wills, K. et al. 2003, *MNRAS*, 342, 861

Treister, E., Urry, C.M., et al., 2004, *ApJ*, 616, 123

Treister, E. & Urry, C.M. 2005, *ApJ*, 630, 15

Ueda, Y., Akiyama, M., Ohta, K., & Miyaji, T. 2003, *ApJ*, 598, 886

Urrutia, T., Lacy, M., Gregg, M.D., & Becker, R.H. 2005, *ApJ*, 627, 75

van Dyk, D. A. et al. 2004, *HEAD*, 8, 1627

Van Duyne, J. et al. 2004, *AAS*, 20516, 309

Vignati, P. et al. 1999, *A&AL*, 349, 57

Xu C., Lonsdale C.J., Shupe D.L., Franceschini A., Martin C., Schiminovich D. 2003, *ApJ*, 587, 90

Webster, R. L., Francis, P. J., Peterson, B. A., Drinkwater, M. J., & Masci, F. J. 1995, *Nature*, 375, 469

Weedman, D. W., Hao, L., Higdon, S. J. U., Devost, D., Wu, Y., Charmandaris, V., Brandl, B., Bass, E., & Houck, J.R. 2005, *ApJ*, 633, 706

Weisskopf, M. C., O'dell, S. L., & van Speybroeck, L. P. 1996, *SPIE*, 2805, 2

Werner, M. W., Roellig, T. L., Low, F. J., Rieke, G. H. et al. 2004, *ApJS*, 154, 1

White, R.L., Helfand, D.J., Becker, R.H., Gregg, M.D., Postman, M., Lauer, T.R., & Oegerle, W. 2003, *AJ*, 126, 706

Wilkes, B. J., Schmidt, G. D., Cutri, R. M., Ghosh, H., Hines, D. C., Nelson, B., Smith, & Paul S. 2002, *ApJ*, 564, 65

Wilson, J. C., Eikenberry, S., Henderson, C., et al. 2003, "A Wide-Field Infrared Camera for the Palomar 200-inch Telescope", *Proceedings of the SPIE*, Volume 4841, pp. 451-458.

Wolf, C., Wisotzki, L., Borch, A., Dye, S., Kleinheinrich, M., & Meisenheimer, K. 2003, *A&AS*, 408, 499

Worsley, M. A., Fabian, A. C., Barcons, X., Mateos, S., Hasinger, G., & Brunner, H. 2004, *MNRAS*, 353, L28

Worsley, M. A., Fabian, A. C., Bauer, F. E., Alexander, D. M., Hasinger, M. S., Brunner, H., Brandt, W. N., & Schneider, D. P. 2005, *MNRAS*, 357, 1281

Zakamska, N.L., Strauss, M. A., Heckman, T. M., Ivezić, Z., Krolik, J. H. 2004, *AJ*, 128, 1002

TABLE 1
SUMMARY OF OBSERVATIONS IN THE *Chandra*/SWIRE SURVEY

Telescope/Instrument	α_{2000} (h m)	δ_{2000} ($^{\circ}$ $'$)	Area	Observing date	Band	Exp. Time (sec)	5σ limit $\mu\text{Jy}/\text{Vega mag}$
KPNO: Mayall 4mt/Mosaic	10 46	+59 00	30' \times 30'	2004 Jan	U	21,600	24.8
KPNO: Mayall 4mt/Mosaic	10 46	+59 03	60' \times 54'	2004 Jan	U	7200	24.3
KPNO: Mayall 4mt/Mosaic	10 46	+59 00	30' \times 30'	2002 Feb	g' , r' , i'	10,800	25.9, 25.2, 24.4
KPNO: Mayall 4mt/Mosaic	10 46	+59 03	60' \times 54'	2002 Feb	g' , r'	3000	25.2, 24.4
KPNO: Mayall 4mt/Mosaic	10 46	+59 03	60' \times 54'	2002 Feb	i'	1800	23.5
KPNO: Mayall 4mt/Mosaic	10 46	+58 33	60' \times 6'	2002 Feb	g' , r' , i'	1800	23.7, 23.5, 22.9
Palomar: 200'' Hale/WIRC	10 46	+59 00	36' \times 43'	2004 Mar 29	K_s	4320	20.5
VLA	10 46	+59 01	40' \times 40'	2001, 2002 & 2003	20 cm	500,000	13.5
<i>Chandra</i> /ACIS-I	10 46	+59 01	47' \times 47'	2004 Sep 12-26	0.3-8 keV	70,000	10^{-15} $\text{ergs cm}^{-2} \text{s}^{-1}$
<i>Spitzer</i> /IRAC	10 45	+58 00	3.69° \times 3.01°	2003 Dec & 2004 Apr	3.6, 4.5, 5.8, 8.0 μm	120-480	5, 9, 43, 40
<i>Spitzer</i> /MIPS	10 45	+58 00	3.66° \times 3.00°	2003 Dec & 2004 May	24 μm	160-360	230

TABLE 2
PROPERTIES OF X-RAY SELECTED COMPTON-THICK AGN

Source name	α_{2000}^a (degrees)	δ_{2000}^a (degrees)	mag(r') (Vega)	$F_{3.6\mu\text{m}}$ (μJy)	$F_{4.5\mu\text{m}}$ (μJy)	$F_{5.8\mu\text{m}}$ (μJy)	$F_{8.0\mu\text{m}}$ (μJy)	$F_{24\mu\text{m}}$ (μJy)	F_{20cm}^b (μJy)
SWIRE_J104311.22+591128.2	160.79675	59.191170	22.81	20	20	<43	<40	<230	<87
SWIRE_J104322.07+590648.7	160.84196	59.113541	24.83	26	29	<43	<40	<230	64 ± 17
SWIRE_J104406.30+583954.1	161.02626	58.665039	23.35	53	67	131	244	1099	<162
SWIRE_J104407.67+584011.3	161.03194	58.669800	>25.2	30	34	<43	<40	<230	<154
SWIRE_J104409.95+585224.8	161.04146	58.873550	23.55	65	152	401	1082	4011	273 ± 15

NOTE.—Typical uncertainties to the IR fluxes are around 10% of the measured fluxes and to the optical magnitudes are around 0.04 mag.

^aIR coordinates

^bUpper limits correspond to 5σ .

TABLE 3
X-RAY PROPERTIES OF X-RAY SELECTED COMPTON-THICK AGN

Source name	α_{2000}^{a} (degrees)	δ_{2000}^{a} (degrees)	Total counts (0.3-8 keV)	Flux ^b (0.3-8 keV)	Flux ^b (0.3-2.5 keV)	Flux ^b (2.5-8 keV)	HR	z_{phot}	$\text{N}_{\text{H}}^{\text{obs}}$	$\text{N}_{\text{H}}^{\text{rest}}$	Log(L) ^e
SWIRE_J104311.22+591128.2	160.79686	59.191322	12 \pm 5	20 \pm 8	0 \pm 3	38 \pm 15	1.00 $^{+0.0}_{-0.15}$	2.27	$>30^{+40}_{-23}$	863 $^{+1151}_{-662}$	45.9
SWIRE_J104322.07+590648.7	160.84201	59.113667	16 \pm 5	25 \pm 9	0 \pm 3	50 \pm 17	1.00 $^{+0.0}_{-0.04}$	1.41	$>30^{+\text{inf}}_{-10}$	312 $^{+\infty}_{-104}$	45.5
SWIRE_J104406.30+583954.1	161.02638	58.665276	22 \pm 6	37 \pm 11	4 \pm 4	63 \pm 20	0.61 $^{+0.21}_{-0.23}$	2.43 ^f	4 $^{+3}_{-1}$	99 $^{+74}_{-25}$	45.7
SWIRE_J104407.67+584011.3	161.03212	58.670094	12 \pm 5	21 \pm 9	0 \pm 3	41 \pm 17	1.00 $^{+0.0}_{-0.13}$	1.42	$>20^{+\text{inf}}_{-11}$	$>200^{+\infty}_{-109}$	45.4
SWIRE_J104409.95+585224.8	161.04143	58.873802	11 \pm 5	19 \pm 8	2 \pm 3	33 \pm 15	0.85 $^{+0.06}_{-0.39}$	2.54 ^f	8 $^{+2}_{-5}$	214 $^{+54}_{-134}$	45.6

^aX-ray coordinates

^bX-ray flux in 10^{-16} ergs cm $^{-2}$ s $^{-1}$ derived assuming an absorbed power-law model with photon index, Γ equal to 1.7 and Galactic N_H (6×10^{19} cm $^{-2}$). Uncertainties reflect only the statistical errors from the observed counts and do not include uncertainties in the spectral model.

^cN_H in the observer rest-frame in 10^{22} cm $^{-2}$.

^dN_H in the source rest-frame in 10^{22} cm $^{-2}$.

^eLogarithm of the 0.3-8 keV absorption-corrected rest-frame luminosity in ergs s $^{-1}$.

^fSpectroscopic z . Photometric z are reported in Table 4.

TABLE 4
PROPERTIES IR-SELECTED OBSCURED AGN CANDIDATES

Source name	α^a (degrees)	δ^a (degrees)	mag(r') (Vega)	$F_{3.6\mu\text{m}}$ (μJy)	$F_{4.5\mu\text{m}}$ (μJy)	$F_{5.8\mu\text{m}}$ (μJy)	$F_{8.0\mu\text{m}}$ (μJy)	$F_{24\mu\text{m}}$ (μJy)	$F_{20\text{cm}}$ (μJy)	z_{spec}	z_{phot}	Class ^b
SWIRE_J104314.93+585606.3	160.81221	58.935070	>24.4	9	22	63	116	936	90±23	...	3.07	I
SWIRE_J104409.95+585224.8	161.04146	58.873550	23.55	65	152	401	1082	4011	273±15	2.540	2.67	I ^c
SWIRE_J104531.45+591027.0	161.38103	59.174160	>25.2	28	54	110	179	1189	103±5	...	1.97	I ^c
SWIRE_J104605.11+584310.8	161.52130	58.719662	>25.2	14	26	59	162	707	58±11	...	2.03	I
SWIRE_J104605.54+583742.5	161.52309	58.628460	>24.4	12	21	72	127	1359	<91	...	3.63	I
SWIRE_J104633.45+590016.7	161.63937	59.004631	>25.2	17	35	67	131	355	33±3	...	1.50	I
SWIRE_J104659.42+584624.1	161.74757	58.773350	>25.2	27	50	77	128	538	223±16	...	1.18	I
SWIRE_J104811.23+592206.8	162.04680	59.368561	>24.4	53	96	181	319	1315	<198	...	1.32	I
SWIRE_J104825.76+591338.9	162.10732	59.227470	>24.4	45	70	150	241	1234	154±23	...	1.31	I ^c
SWIRE_J104301.13+591214.4	160.75470	59.204010	>24.4	36	61	109	150	1022	185±44	...	2.16	II
SWIRE_J104310.29+585916.0	160.79289	58.987789	23.78	24	33	50	87	548	<68	...	2.00	II ^c
SWIRE_J104311.81+590649.9	160.79923	59.113850	22.97	129	210	428	714	1921	<217	...	0.83	II
SWIRE_J104323.61+590218.3	160.84839	59.038422	24.40	25	27	33	54	326	<146	...	0.90	II
SWIRE_J104359.77+585811.3	160.99904	58.969810	>25.2	14	17	<43	53	358	<27	...	2.35	II
SWIRE_J104402.02+584504.9	161.00841	58.751362	23.65	44	48	58	112	882	<30	...	2.04	II
SWIRE_J104406.30+583954.1	161.02626	58.665039	23.35	53	67	131	244	1099	<162	2.430	2.14	II ^c
SWIRE_J104406.71+585130.8	161.02797	58.858551	24.90	24	28	<43	66	397	<94	...	1.99	II ^c
SWIRE_J104423.99+584638.3	161.09996	58.777302	24.82	15	24	30	64	307	<119	...	0.88	II
SWIRE_J104444.84+585019.5	161.18681	58.838749	24.63	14	16	<43	52	440	55±8	...	3.42	II
SWIRE_J104458.45+590314.0	161.24353	59.053890	23.42	93	157	328	623	1861	33±4	1.520	1.58	II
SWIRE_J104459.07+590705.3	161.24612	59.118141	23.68	31	45	58	132	674	40±4	...	0.89	II
SWIRE_J104524.91+591626.7	161.35379	59.274071	24.69	35	47	59	106	636	140±15	...	0.72	II
SWIRE_J104525.21+585949.3	161.35506	58.997040	>25.2	10	19	39	64	335	24±3	...	2.05	II ^c
SWIRE_J104533.47+590541.1	161.38947	59.094749	24.60	13	15	37	52	398	33±3	...	2.77	II
SWIRE_J104551.81+590345.3	161.46588	59.062592	24.06	34	41	53	88	472	21±5	...	1.00	II ^c
SWIRE_J104554.47+592322.2	161.47697	59.389488	>24.4	9	19	33	89	242	<216	...	3.48	II
SWIRE_J104604.78+591625.3	161.51993	59.273701	23.80	38	66	115	193	538	<72	...	1.13	II
SWIRE_J104609.55+590849.0	161.53979	59.146938	24.09	17	27	45	101	319	44±3	...	1.82	II
SWIRE_J104622.31+585036.0	161.59294	58.843330	23.79	36	53	74	143	509	79±12	...	0.96	II
SWIRE_J104627.46+584049.2	161.61443	58.680328	24.04	26	42	57	150	488	<154	...	0.81	II
SWIRE_J104633.29+584820.3	161.63870	58.805641	24.05	17	20	32	47	440	47±6	...	2.69	II ^c
SWIRE_J104637.25+585252.4	161.65520	58.881222	>25.2	14	25	48	99	332	25±4	...	1.84	II
SWIRE_J104637.57+590014.6	161.65654	59.004059	>25.2	10	12	<43	32	418	24±7	...	3.43	II
SWIRE_J104657.15+592152.8	161.73814	59.364658	24.04	28	31	51	64	698	<89	1.579	2.56	II
SWIRE_J104658.67+584042.4	161.74446	58.678440	>24.4	30	47	61	105	269	192±43	...	1.32	II
SWIRE_J104700.21+590107.6	161.75087	59.018780	23.72	28	33	59	158	1273	279±6	2.562	2.85	II
SWIRE_J104704.98+585849.7	161.77074	59.980469	24.18	27	33	55	74	427	<35	...	2.09	II
SWIRE_J104705.31+584420.3	161.77211	58.738960	23.47	37	49	66	87	738	219±23	...	2.25	II
SWIRE_J104705.49+590919.4	161.77287	59.155380	25.06	16	30	66	111	903	53±6	...	2.44	II
SWIRE_J104714.84+591916.5	161.81181	59.321259	23.98	41	54	65	94	862	262±36	...	0.76	II
SWIRE_J104726.03+591305.5	161.85844	59.218189	>25.2	26	41	68	114	409	169±16	...	1.67	II
SWIRE_J104735.76+584707.3	161.89902	58.785370	>25.2	12	17	32	56	313	89±12	...	2.11	II
SWIRE_J104735.93+590549.7	161.89970	59.097149	24.74	21	29	54	67	324	<55	...	1.64	II ^c
SWIRE_J104746.64+585113.5	161.94432	58.853760	>25.2	11	20	32	50	244	41±10	...	1.85	II
SWIRE_J104746.79+591759.2	161.94496	59.299770	24.59	21	27	<43	62	393	<196	...	2.09	II
SWIRE_J104754.20+590956.3	161.97582	59.165630	23.84	22	26	<43	58	448	<91	...	2.57	II
SWIRE_J104806.02+584456.4	162.02510	58.749001	24.34	25	33	<43	52	338	126±24	...	0.81	II
SWIRE_J104820.64+592436.6	162.08600	59.410160	23.75	25	42	76	196	833	<1064	...	2.46	II
SWIRE_J104831.65+592004.6	162.13188	59.334621	22.87	68	73	87	147	775	<596	...	0.60	II
SWIRE_J104836.72+585414.7	162.15300	58.904072	22.77	75	117	161	231	887	<176	...	0.53	II ^c
SWIRE_J104844.25+585139.4	162.18439	58.860931	>24.4	15	24	<43	64	200	<248	...	1.54	II
SWIRE_J104903.66+590006.9	162.26524	59.001930	24.24	29	42	51	119	379	<276	...	1.64	II ^c
SWIRE_J104955.03+584742.8	162.47929	58.795219	23.10	22	31	43	125	1080	3.42	II
SWIRE_J104257.62+590438.9	160.74010	59.077469	23.39	21	23	<43	40	256	<281	...	1.54	III
SWIRE_J104321.34+590943.0	160.83891	59.161942	20.03	184	239	345	492	2665	<209	...	2.29	III ^c

TABLE 4—Continued

Source name	α^a (degrees)	δ^a (degrees)	mag(r') (Vega)	$F_{3.6\mu\text{m}}$ (μJy)	$F_{4.5\mu\text{m}}$ (μJy)	$F_{5.8\mu\text{m}}$ (μJy)	$F_{8.0\mu\text{m}}$ (μJy)	$F_{24\mu\text{m}}$ (μJy)	$F_{20\text{cm}}$ (μJy)	z_{spec}	z_{phot}	Class ^b
SWIRE_J104353.42+585316.2	160.97260	58.887840	22.75	32	39	62	90	560	<103	0.563	0.69	III ^c
SWIRE_J104359.52+590156.3	160.99800	59.032310	23.25	34	58	84	148	464	103±8	...	0.84	III
SWIRE_J104414.18+584644.6	161.05907	58.779049	22.26	63	81	126	268	1762	435±25	...	2.73	III
SWIRE_J104432.03+590457.7	161.13344	59.082691	22.80	56	111	192	339	1067	104±8	...	0.90	III ^c
SWIRE_J104447.56+585918.7	161.19815	58.988529	22.90	29	38	66	127	660	120±4	2.488	2.44	III
SWIRE_J104500.71+591353.4	161.25297	59.231491	23.13	45	70	108	156	776	64±13	...	0.70	III ^c
SWIRE_J104528.33+583651.8	161.36803	58.614391	22.12	24	37	54	87	366	<325	...	1.54	III
SWIRE_J104616.93+585457.1	161.57056	58.915871	23.63	26	32	<43	52	241	60±7	...	0.70	III ^c
SWIRE_J104635.87+590748.8	161.64946	59.130219	23.48	39	48	58	67	615	97±3	...	0.45	III
SWIRE_J104638.87+591931.4	161.66196	59.325378	>24.4	9	16	<43	71	227	<124	...	2.09	III
SWIRE_J104641.38+585213.9	161.67242	58.870529	22.75	42	84	204	541	2797	1004±8	...	1.10	III ^c
SWIRE_J104644.18+590027.8	161.68407	59.007710	22.56	33	42	67	77	899	30±6	2.542	2.79	III ^c
SWIRE_J104733.37+591200.9	161.88902	59.200241	22.39	91	127	196	307	1110	49±9	...	0.71	III
SWIRE_J104748.20+590905.7	161.95082	59.151581	23.48	25	33	50	63	375	<78	...	3.14	III
SWIRE_J104749.61+584845.7	161.95670	58.812691	23.03	25	32	39	58	183	<114	...	0.69	III ^c
SWIRE_J104826.99+585438.8	162.11246	58.910782	22.89	32	53	84	156	519	87±14	...	1.41	III ^c
SWIRE_J104913.37+585946.3	162.30569	58.996181	23.41	22	27	38	88	316	<356	...	3.43	III ^c
SWIRE_J104229.75+591154.6	160.62396	59.198490	>24.4	36	51	52	114	983	<281	...	1.89	IV
SWIRE_J104241.45+591357.2	160.67270	59.232559	>24.4	31	43	44	124	319	<816	...	1.43	IV ^c
SWIRE_J104254.46+591013.3	160.72691	59.170361	>24.4	47	61	63	152	591	<411	...	1.54	IV ^c
SWIRE_J104414.37+584320.4	161.05988	58.722340	>25.2	65	79	90	149	1061	754±22	...	1.78	IV
SWIRE_J104420.22+583948.0	161.08424	58.663342	24.89	44	62	71	104	615	<346	...	1.70	IV ^c
SWIRE_J104526.75+583526.0	161.36145	58.590542	>23.5	104	104	126	349	2538	622±45	...	1.84	IV
SWIRE_J104528.29+591326.7	161.36789	59.224079	23.45	35	47	91	199	2410	14379±10	...	0.67	IV ^c
SWIRE_J104650.27+592602.8	161.70947	59.434120	>24.4	31	48	67	203	1488	<147	...	0.88	IV
SWIRE_J104718.10+585526.2	161.82542	58.923931	>25.2	11	16	<43	29	314	60±5	...	1.95	IV
SWIRE_J104733.46+592108.1	161.88942	59.352242	23.88	44	52	75	199	801	92±30	...	1.11	IV ^c
SWIRE_J104734.47+591329.1	161.89362	59.225819	>25.2	13	17	<43	42	356	94±10	...	1.90	IV
SWIRE_J104736.92+591941.3	161.90385	59.328152	>24.4	31	37	53	93	383	<220	...	1.54	IV ^c
SWIRE_J104754.78+590810.4	161.97826	59.136211	>25.2	11	18	<43	34	274	<26	...	1.83	IV ^c
SWIRE_J104802.42+592656.5	162.01010	59.449020	>24.4	36	42	58	83	1043	<423	...	2.14	IV
SWIRE_J104813.49+590340.7	162.05620	59.061310	>24.4	13	21	<43	46	356	41±10	...	1.82	IV ^c
SWIRE_J104838.01+591702.6	162.15836	59.284050	>24.4	18	22	28	63	430	<438	...	1.79	IV
SWIRE_J104303.50+585718.1	160.76460	58.955029	20.32	322	364	611	1136	5371	<244	...	0.60	V ^c
SWIRE_J104351.87+584953.7	160.96614	58.831589	23.02	23	27	57	103	996	<139	0.609	0.59	V ^c
SWIRE_J104407.97+584437.0	161.03319	58.743622	20.32	655	858	1148	1595	7053	213±48	0.555	0.58	V ^c
SWIRE_J104422.64+591304.1	161.09435	59.217819	21.49	145	176	262	352	1439	123±17	...	0.32	V ^c
SWIRE_J104503.56+585109.9	161.26485	58.852741	22.83	133	176	237	344	1006	86±19	...	0.98	V ^c
SWIRE_J104504.96+585947.3	161.27066	58.996479	21.15	80	89	136	309	2404	137±11	0.214	0.13	V ^c
SWIRE_J104532.93+584638.6	161.38722	58.777382	24.37	34	45	64	124	345	<66	...	1.78	V ^c
SWIRE_J104704.33+591142.9	161.76802	59.195240	>25.2	21	25	41	55	185	<57	...	1.34	V
SWIRE_J104708.05+585026.3	161.78352	58.840641	20.79	79	101	144	242	1607	<58	...	0.44	V
SWIRE_J104725.94+591025.5	161.85806	59.173759	21.54	111	150	200	277	886	73±7	...	0.67	V ^c
SWIRE_J104731.84+592432.9	161.88266	59.409149	>24.4	31	38	54	76	281	<483	...	3.11	V ^c
SWIRE_J104734.57+584338.7	161.89404	58.727409	22.68	105	119	180	302	1286	118±21	...	0.87	V
SWIRE_J104748.27+590534.7	161.95113	59.092960	>25.2	16	19	26	41	<230	199±7	...	1.04	V ^c
SWIRE_J104826.92+592116.1	162.11218	59.354469	20.08	258	316	423	738	3632	450±79	...	0.58	V
SWIRE_J104829.49+591249.1	162.12288	59.213631	21.07	108	155	208	333	1117	125±23	...	0.28	V ^c
SWIRE_J104851.80+591019.8	162.21584	59.172161	22.87	60	97	137	196	957	<295	...	0.82	V
SWIRE_J104344.33+585102.5	160.93469	58.850689	>24.4	9	16	<43	<40	260	<144	...	2.01	VI
SWIRE_J104407.69+585125.9	161.03204	58.857189	>25.2	6	9	<43	<40	341	<93	...	2.51	VI
SWIRE_J104408.30+590455.4	161.03458	59.082062	>25.2	9	13	<43	<40	240	<67	...	1.79	VI
SWIRE_J104530.65+585936.8	161.37772	58.993549	>25.2	10	13	<43	<40	256	19±3	...	1.93	VI
SWIRE_J104534.22+591400.3	161.39259	59.233410	>25.2	8	13	<43	<40	277	<56	...	1.91	VI
SWIRE_J104558.79+583812.9	161.49496	58.636909	>24.4	8	13	<43	<40	344	<233	...	2.73	VI

TABLE 4—Continued

Source name	α^a (degrees)	δ^a (degrees)	mag(r') (Vega)	$F_{3.6\mu\text{m}}$ (μJy)	$F_{4.5\mu\text{m}}$ (μJy)	$F_{5.8\mu\text{m}}$ (μJy)	$F_{8.0\mu\text{m}}$ (μJy)	$F_{24\mu\text{m}}$ (μJy)	$F_{20\text{cm}}$ (μJy)	z_{spec}	z_{phot}	Class ^b
SWIRE_J104623.23+584410.9	161.59677	58.736351	>25.2	9	14	<43	<40	280	<90	...	2.61	VI
SWIRE_J104632.92+590820.9	161.63716	59.139141	>25.2	10	15	<43	<40	245	36±4	...	1.75	VI
SWIRE_J104703.99+585039.9	161.76662	58.844410	24.79	8	14	<43	<40	263	<55	...	2.06	VI
SWIRE_J104708.15+585721.1	161.78397	58.955860	>25.2	10	17	<43	<40	240	<38	...	1.93	VI
SWIRE_J104708.92+584524.1	161.78716	58.756691	>25.2	9	13	<43	<40	299	<102	...	1.95	VI
SWIRE_J104720.43+590107.9	161.83514	59.018871	>25.2	8	12	<43	<40	260	39±4	...	1.93	VI
SWIRE_J104728.64+585346.1	161.86932	58.896141	24.02	14	19	<43	41	<230	<57	...	0.58	VI
SWIRE_J104747.72+585903.9	161.94882	58.984421	>25.2	6	9	<43	<40	243	122±7	...	2.09	VI
SWIRE_J104754.71+591137.2	161.97797	59.193661	>25.2	10	14	<43	<40	254	<106	...	1.82	VI
SWIRE_J104803.66+592252.5	162.01524	59.381248	>24.4	8	14	<43	<40	259	<564	...	2.17	VI

NOTE.—Typical uncertainties to the IR fluxes are $\sim 10\%$ of the measured fluxes and to the optical magnitudes are around 0.04 mag. Upper limits correspond to 5σ values.

^aIR coordinates

^bClass I sources are characterized by convex IR SED fitted by a “Torus” template. Class II sources show power-law like optical-IR SEDs, similar to Mrk 231 or slightly redder ($A_V < 1$). Class III sources have power-law like optical-IR SED fitted by a reddened QSO template ($A_V = 0.6\text{--}1.0$). Class IV sources show signatures from both a starburst and an AGN component. Class V sources are characterized by very red optical SEDs and power-law like IR SEDs. Class VI objects are detected only in three bands from 3.6 to $24\mu\text{m}$.

^cX-ray source

TABLE 5
X-RAY PROPERTIES OF IR-SELECTED AGN

Source name	Total counts (0.3-8 keV)	$F_{0.3-8\text{keV}}^{\text{a}}$	$F_{0.3-2.5\text{keV}}^{\text{a}}$	$F_{2.5-8\text{keV}}^{\text{a}}$	HR	z	$N_{\text{H}}^{\text{obsb}}$	$N_{\text{H}}^{\text{restc}}$	$\text{Log}(L)^{\text{d}}$	Class
SWIRE_J104409.95+585224.8	11 \pm 5	19 \pm 8	2 \pm 3	33 \pm 15	0.85 $^{+0.06}_{-0.20}$	2.540 ^f	8.0	214.0	45.637	I
SWIRE_J104531.45+591027.0	7 \pm 4	12 \pm 7	5 \pm 4	10 \pm 11	-0.14 $^{+0.76}_{-0.84}$	1.973	0.7	11.6	43.986	I
SWIRE_J104825.76+591338.9	21 \pm 7	34 \pm 12	19 \pm 7	13 \pm 16	-0.61 $^{+0.45}_{-0.00}$	1.307	<0.1	0.1	43.497	I
SWIRE_J104310.29+585916.0	118 \pm 13	202 \pm 22	84 \pm 12	162 \pm 30	-0.20 $^{+0.20}_{-0.20}$	1.997	0.6	10.0	45.186	II
SWIRE_J104406.30+583954.1	22 \pm 6	37 \pm 11	4 \pm 4	63 \pm 20	0.61 $^{+0.21}_{-0.23}$	2.430 ^f	4.3	99.0	45.738	II
SWIRE_J104406.71+585130.8	10 \pm 5	17 \pm 8	10 \pm 5	4 \pm 10	-0.78 $^{+0.38}_{-0.33}$	1.991	<0.1	0.2	43.645	II
SWIRE_J104525.21+585949.3	16 \pm 5	27 \pm 9	15 \pm 6	10 \pm 12	-0.62 $^{+0.34}_{-0.18}$	2.045	<0.1	0.2	43.882	II
SWIRE_J104551.81+590345.3	10 \pm 5	17 \pm 8	5 \pm 4	19 \pm 13	0.10 $^{+0.56}_{-0.62}$	0.999	1.3	7.8	43.363	II
SWIRE_J104633.29+584820.3	6 \pm 4	10 \pm 7	5 \pm 4	6 \pm 10	-0.40 $^{+0.37}_{-0.00}$	2.693	0.2	6.4	44.102	II
SWIRE_J104735.93+590549.7	34 \pm 7	55 \pm 11	21 \pm 6	48 \pm 16	-0.12 $^{+0.20}_{-0.19}$	1.644	0.8	9.4	44.412	II
SWIRE_J104836.72+585414.7	59 \pm 9	98 \pm 15	54 \pm 9	39 \pm 16	-0.60 $^{+0.13}_{-0.11}$	0.533	<0.1	<0.1	43.002	II
SWIRE_J104903.66+590006.9	19 \pm 7	32 \pm 12	21 \pm 7	4 \pm 16	-0.87 $^{+0.38}_{-0.00}$	1.641	<0.1	0.1	43.716	II
SWIRE_J104321.34+590943.0	1227 \pm 36	1980 \pm 58	993 \pm 34	1092 \pm 63	-0.45 $^{+0.02}_{-0.03}$	2.294	0.1	2.9	46.108	III
SWIRE_J104353.42+585316.2	49 \pm 8	84 \pm 14	25 \pm 7	95 \pm 22	0.14 $^{+0.16}_{-0.16}$	0.563 ^f	1.4	4.5	43.380	III
SWIRE_J104432.03+590457.7	134 \pm 14	230 \pm 23	83 \pm 12	221 \pm 34	-0.04 $^{+0.18}_{-0.18}$	0.896	0.9	4.9	44.308	III
SWIRE_J104500.71+591353.4	16 \pm 5	29 \pm 9	9 \pm 5	32 \pm 15	0.11 $^{+0.30}_{-0.30}$	0.700	1.3	5.3	43.161	III
SWIRE_J104616.93+585457.1	49 \pm 8	84 \pm 15	37 \pm 8	62 \pm 19	-0.27 $^{+0.26}_{-0.26}$	0.705	0.4	1.8	43.494	III
SWIRE_J104641.38+585213.9	12 \pm 5	19 \pm 8	9 \pm 5	14 \pm 12	-0.26 $^{+0.48}_{-0.49}$	1.095	0.4	3.1	43.367	III
SWIRE_J104644.18+590027.8	33 \pm 7	56 \pm 12	23 \pm 7	46 \pm 17	-0.19 $^{+0.26}_{-0.24}$	2.542 ^f	0.6	15.7	44.976	III
SWIRE_J104749.61+584845.7	45 \pm 8	75 \pm 14	39 \pm 8	37 \pm 16	-0.50 $^{+0.24}_{-0.20}$	0.695	0.05	0.2	43.237	III
SWIRE_J104826.99+585438.8	16 \pm 5	27 \pm 9	8 \pm 5	30 \pm 14	0.10 $^{+0.28}_{-0.31}$	1.410	1.3	12.8	44.019	III
SWIRE_J104913.37+585946.3	39 \pm 9	65 \pm 15	21 \pm 7	70 \pm 23	0.07 $^{+0.26}_{-0.18}$	3.435	1.2	58.8	45.861	III
SWIRE_J104241.45+591357.2	28 \pm 7	45 \pm 12	23 \pm 7	22 \pm 15	-0.51 $^{+0.26}_{-0.22}$	1.434	0.04	0.4	43.812	IV
SWIRE_J104254.46+591013.3	32 \pm 7	52 \pm 11	18 \pm 6	53 \pm 17	0.03 $^{+0.21}_{-0.21}$	1.541	1.1	12.3	44.385	IV
SWIRE_J104420.22+583948.0	56 \pm 9	97 \pm 15	30 \pm 7	107 \pm 23	0.11 $^{+0.16}_{-0.16}$	1.700	1.3	17.5	44.842	IV
SWIRE_J104528.29+591326.7	18 \pm 5	31 \pm 10	9 \pm 5	35 \pm 15	0.16 $^{+0.27}_{-0.28}$	0.669	1.5	5.5	43.153	IV
SWIRE_J104733.46+592108.1	40 \pm 8	70 \pm 13	40 \pm 8	24 \pm 14	-0.65 $^{+0.15}_{-0.12}$	1.107	<0.1	0.1	43.628	IV
SWIRE_J104736.92+591941.3	9 \pm 4	15 \pm 8	9 \pm 5	6 \pm 10	-0.60 $^{+0.63}_{-0.00}$	1.543	<0.1	0.1	43.332	IV
SWIRE_J104754.78+590810.4	16 \pm 5	25 \pm 9	14 \pm 5	11 \pm 11	-0.57 $^{+0.28}_{-0.24}$	1.826	<0.1	0.1	43.728	IV
SWIRE_J104813.49+590340.7	17 \pm 5	28 \pm 9	17 \pm 6	6 \pm 10	-0.79 $^{+0.21}_{-0.14}$	1.818	<0.1	0.1	43.769	IV
SWIRE_J104303.50+585718.1	14 \pm 7	24 \pm 11	3 \pm 5	38 \pm 19	0.60 $^{+0.62}_{-0.70}$	0.595	3.6	12.0	43.073	V
SWIRE_J104351.87+584953.7	44 \pm 8	75 \pm 14	10 \pm 5	121 \pm 25	0.61 $^{+0.25}_{-0.31}$	0.609 ^f	3.6	12.5	43.605	V
SWIRE_J104407.97+584437.0	48 \pm 8	83 \pm 14	30 \pm 8	81 \pm 21	-0.03 $^{+0.20}_{-0.20}$	0.555 ^f	1.0	3.0	43.306	V
SWIRE_J104422.64+591304.1	800 \pm 29	1292 \pm 48	649 \pm 28	711 \pm 52	-0.45 $^{+0.09}_{-0.08}$	0.323	0.1	0.3	43.730	V
SWIRE_J104503.56+585109.9	29 \pm 8	49 \pm 14	18 \pm 7	45 \pm 20	-0.08 $^{+0.29}_{-0.28}$	0.981	0.8	4.9	43.729	V
SWIRE_J104504.96+585947.3	59 \pm 9	102 \pm 16	3 \pm 5	193 \pm 31	0.90 $^{+0.06}_{-0.14}$	0.214 ^f	8.7	14.3	42.736	V
SWIRE_J104532.93+584638.6	101 \pm 12	176 \pm 20	98 \pm 12	69 \pm 22	-0.60 $^{+0.18}_{-0.15}$	1.781	<0.1	0.1	44.545	V
SWIRE_J104725.94+591025.5	136 \pm 13	219 \pm 21	116 \pm 13	102 \pm 23	-0.54 $^{+0.10}_{-0.10}$	0.668	<0.1	<0.1	43.585	V
SWIRE_J104731.84+592432.9	31 \pm 7	55 \pm 12	24 \pm 7	40 \pm 17	-0.28 $^{+0.24}_{-0.22}$	3.108	0.4	16.6	45.174	V
SWIRE_J104748.27+590534.7	15 \pm 5	24 \pm 9	12 \pm 5	14 \pm 12	-0.43 $^{+0.38}_{-0.32}$	1.041	0.2	1.1	43.292	V

TABLE 5—*Continued*

Source name	Total counts (0.3-8 keV)	$F_{0.3-8\text{keV}}^{\text{a}}$	$F_{0.3-2.5\text{keV}}^{\text{a}}$	$F_{2.5-8\text{keV}}^{\text{a}}$	HR	z	$N_{\text{H}}^{\text{obsb}}$	$N_{\text{H}}^{\text{restc}}$	$\log(L)^{\text{d}}$	Class
SWIRE_J104829.49+591249.1	67 ± 10	108 ± 16	50 ± 9	72 ± 21	$-0.33^{+0.24}_{-0.22}$	0.280	0.3	0.6	42.577	V

^aX-ray flux in $10^{-16} \text{ ergs cm}^{-2} \text{ s}^{-1}$ derived assuming an absorbed power-law model with photon index, Γ equal to 1.7 and Galactic N_{H} ($6 \times 10^{19} \text{ cm}^{-2}$). Uncertainties reflect only the statistical errors from the observed counts and do not include uncertainties in the spectral model.

^b N_{H} in the observer rest-frame in 10^{22} cm^{-2} .

^c N_{H} in the source rest-frame in 10^{22} cm^{-2} .

^dLogarithm of the 0.3-8 keV absorption-corrected rest-frame luminosity in ergs s^{-1} .

^eSpectroscopic z . Photometric z are reported in Table 4.

TABLE 6
PHOTOMETRIC DATA FOR SW104409

Observed Bandpass	Rest-frame Bandpass	Magnitude (Vega)	Flux Density (erg cm ⁻² s ⁻¹ /μJy)	Instrument
0.3–2.5 keV	1.1–8.8 keV	...	(22±3)×10 ⁻¹⁶	<i>Chandra</i> /ACIS
2.5–8.0 keV	8.8–28.3 keV	...	(33±15)×10 ⁻¹⁶	<i>Chandra</i> /ACIS
0.3–8.0 keV	1.1–28.3 keV	...	(19±8)×10 ⁻¹⁶	<i>Chandra</i> /ACIS
<i>U</i> 3647 Å	1031 Å	24.29±0.10	0.369±0.033	KPNO/Mosaic
<i>g'</i> 4782 Å	1351 Å	24.00±0.07	0.983±0.060	KPNO/Mosaic
<i>r'</i> 6288 Å	1777 Å	23.55±0.04	1.166±0.040	KPNO/Mosaic
<i>i'</i> 7665 Å	2166 Å	23.22±0.07	1.279±0.071	KPNO/Mosaic
<i>K_s</i> 2.153 μm	6085 Å	19.37±0.14	10.55±1.42	Palomar/WIRC
3.6 μm	1.01 μm	...	65.5±0.9	<i>Spitzer</i> /IRAC
4.5 μm	1.27 μm	...	152±2	<i>Spitzer</i> /IRAC
5.8 μm	1.61 μm	...	401±5	<i>Spitzer</i> /IRAC
8.0 μm	2.25 μm	...	1082±6	<i>Spitzer</i> /IRAC
24. μm	6.74 μm	...	4011±20	<i>Spitzer</i> /MIPS
1.4 GHz	4.95 GHz	...	273±15	VLA

TABLE 7
PHOTOMETRIC DATA FOR SW104406

Observed Bandpass	Rest-frame Bandpass	Magnitude (Vega)	Flux Density (erg cm ⁻² s ⁻¹ /μJy)	Instrument
0.3–2.5 keV	1.03–8.6 keV	...	(4±4)×10 ⁻¹⁶	<i>Chandra</i> /ACIS
2.5–8.0 keV	8.6–27.4 keV	...	(63±20)×10 ⁻¹⁶	<i>Chandra</i> /ACIS
0.3–8.0 keV	1.03–27.4 keV	...	(37±10)×10 ⁻¹⁶	<i>Chandra</i> /ACIS
<i>U</i> 3647 Å	1063 Å	24.27±0.17	0.376±0.033	KPNO/Mosaic
<i>g'</i> 4782 Å	1394 Å	23.68±0.05	1.323±0.060	KPNO/Mosaic
<i>r'</i> 6288 Å	1833 Å	23.35±0.06	1.407±0.040	KPNO/Mosaic
<i>i'</i> 7665 Å	2235 Å	22.76±0.13	1.954±0.071	KPNO/Mosaic
<i>K_s</i> 2.153 μm	6278 Å	18.59±0.17	24.52±3.25	Palomar/WIRC
3.6 μm	1.04 μm	...	53.4±1.3	<i>Spitzer</i> /IRAC
4.5 μm	1.31 μm	...	67.6±1.2	<i>Spitzer</i> /IRAC
5.8 μm	1.66 μm	...	131±7	<i>Spitzer</i> /IRAC
8.0 μm	2.32 μm	...	244±5	<i>Spitzer</i> /IRAC
24. μm	6.95 μm	...	1099±18	<i>Spitzer</i> /MIPS
1.4 GHz	4.95 GHz	...	<162	VLA

TABLE 8
EMISSION-LINE MEASUREMENTS OF SW104409

Line	λ_{obs} (Å)	Redshift	Flux (10^{-16} ergs cm $^{-2}$ s $^{-1}$)	FWHM (km s $^{-1}$)	$W_{\lambda,\text{rest}}$ (Å)
Ly α ^a	4304.5	2.540	12.5 ± 1.3	1324 ± 80	105 ± 11
N V $\lambda 1240^{\text{a}}$	4389.5	2.540	1.88 ± 0.56	1366 ± 300	16 ± 5
C IV $\lambda 1549^{\text{a}}$	5479.3	2.537	2.23 ± 0.45	1367 ± 200	21 ± 4
Ly α /N V $\lambda 1240^{\text{b}}$	23.0 ± 2.3	...	311 ± 31
Si IV/O IV] $\lambda 1400^{\text{b}}$	2.34 ± 0.47	...	29 ± 6
C IV $\lambda 1549^{\text{b}}$	4.15 ± 0.62	...	39 ± 6

NOTE.—Rest-frame equivalent widths $W_{\lambda,\text{rest}}$ assume $z = 2.54$.

^aGaussian fit to narrow component

^bTotal integration.

TABLE 9
EMISSION-LINE MEASUREMENTS OF SW104406

Line	λ_{obs} (Å)	Redshift	Flux (10^{-16} ergs cm $^{-2}$ s $^{-1}$)	FWHM (km s $^{-1}$)	$W_{\lambda,\text{rest}}$ (Å)
Ly α	4171.3	2.431	14.9 ± 1.5	1360 ± 20	184 ± 18
N V $\lambda 1240$	4254.8	2.431	9.82 ± 0.29	2037 ± 40	120 ± 4
Si IV $\lambda 1397$	4777.4	2.430	1.15 ± 0.35	1684 ± 200	16 ± 5
O IV] $\lambda 1402$	4809.4	2.430	1.23 ± 0.12	1120 ± 100	17 ± 2
C IV $\lambda 1549$	5310.7	2.428	7.14 ± 0.14	1485 ± 60	86 ± 2
He II $\lambda 1640$	5618.9	2.425	1.50 ± 0.08	1278 ± 100	20 ± 1

NOTE.—All parameters are derived for Gaussian fits. Rest-frame equivalent widths $W_{\lambda,\text{rest}}$ assume $z = 2.43$.

TABLE 10
X-RAY OBSERVATIONAL DETAILS

Source Name	Sequence No.	OBSID	Date	Exp. Time (ksec)
SW104406	900331	5024	16 Sept 2004	57.97
SW104409	900334	5027	20 Sept 2004	67.96

TABLE 11
LUMINOSITIES AND BLACK-HOLE MASSES OF SW104409 AND SW104406

Source Name	L_{Radio} 1.4 GHz	$L(O - NIR)$ ^a 0.03 – 10 μm	$L(IR)$ ^a 3 – 1000 μm	$L(O - IR)$ ^a 0.03 – 1000 μm	$L(X)$ ^b 0.3 – 8 keV	L_{bol} ^c	M_{BH} ^d 10 ⁸ M_{\odot}	dM/dt ^e M_{\odot}/yr
SW104406	<40.07	45.48	46.08	46.14	45.74	46.29 (45.93)	1.4 (0.7)	3.4 (1.5)
SW104409	40.32	47.19	47.53	47.58	45.64	47.59 (47.21)	29.9 (12.4)	68 (28)

NOTE.—All luminosities are in logarithmic scale and units of ergs s^{-1} . See section 6 for more details.

^aDerived assuming the model shown in Figure 9 for SW104409 and in Figure 11 for SW104406.

^bAbsorption-corrected X-ray luminosity between 0.3 and 8 keV.

^cBolometric luminosity derived as the sum of $L(OIR)$, $L(0.3 - 8\text{keV})$ and $L(Radio)$ if available. The value in parenthesis does not include the luminosity emitted at $\lambda^{rest} > 10\mu m$ and was obtained by replacing $L(O - IR)$ with $L(O - NIR)$ in the L_{bol} calculation.

^dBlack-hole mass derived from L_{bol} and assuming that the source is accreting at the Eddington limit. The value in parenthesis was derived using the L_{bol} value shown in parenthesis in column 7.

^eAccretion rate derived from L_{bol} and assuming that the source is accreting with 10% efficiency. The value in parenthesis was derived using the L_{bol} value shown in parenthesis in column 7.

